Doctorate Dissertation

博士論文

Experimental and theoretical study
on initial stage of oxidation of metal clusters

（金属クラスターの酸化反応初期過程に関する
実験的・理論的研究）

A Dissertation Submitted for Degree of Doctor of Philosophy
December 2018
平成30年12月博士（理学）申請

Department of Chemistry, Graduate School of Science,
The University of Tokyo
東京大学大学院理学系研究科化学専攻

Ryohei Tomihara
冨原　良平

Abstract

Metal clusters have gained much attention as key building units of the novel functional materials due to their size-specific properties. Metal clusters show size-dependency in stability, electronic structure and reactivity. Oxidation reaction of metal cluster is closely related to the key step of the catalytic oxidation reaction via activation of molecular oxygen. Metal clusters show the size-dependent bonding motif and special magic compositions during sequential oxidation reaction.

The aim of the thesis is to obtain fundamental insights into the catalytic oxidation reactions of the metal clusters. I focused on the initial stage of the oxidation reactions of metal clusters in order to shed light on the formation process of the metal oxides in nanoscale. To elucidate abundances and structures of metal oxides produced in the early stage of the oxidation reaction, I combined several experimental and theoretical methods.

In Chapter 1, I describe the general introduction on the size specific properties of metal clusters including reactivity. I also show examples of previous studies on oxidation pathway of metal clusters and on the magic stability and geometric structures of metal oxide clusters. Finally I explain the purpose of this thesis.

In Chapter 2, I investigated the oxidation reaction of the cobalt cluster anions by using mass spectrometry, photoelectron spectroscopy and DFT calculations. Two types of magic behaviors in mass spectra were observed. DFT calculations showed the surface oxidized species of Co cluster with μ_2- and μ_3- bonded oxygen atoms and it suggested that the one magic behavior could be explained by the surface oxidation and full oxidation

to bulk compositions. On the other hand, photoelectron spectra indicated the relatively large increase of the electron affinity of the magic species and it suggested that another magic compositions have low reactivity on the thermionic electron emission so they are stable as anions.

In Chapter 3, I studied the oxidation reaction of the iridium cluster anions by using mass spectrometry, ion mobility spectroscopy and theoretical calculations. According to ion mobility results, Ir_n^- had the characteristic cubic-based structures. In the case of $Ir_nO_m^-$, oxygen atoms were bonded to terminal sites of the cubic-like Ir core as on-top motif, while other metals typically showed the μ_2 bonding motif of oxygen atoms on the bridge site. In addition, $Ir_8O_m^-$ showed the bonding motif transition from on-top to bridging motif due to the core distortion by the sequential oxygen binding.

In Chapter 4, I give a summary of the thesis and describe future prospects as a concluding remark.

Contents

Chapter 1.

General introduction

1.1. Metal clusters

1.1.1. Size dependent properties

Metal cluster is defined as an assembly of a few to hundreds of metal atoms through direct metal-metal bondings.[1] Metal clusters have gained much attention as key building units of the novel functional materials due to their size-specific properties resulted from the discrete electronic structures and the unique geometric structures. For example, mass spectrometric studies have shown that the relative stabilities of metal clusters are strongly dependent on size and are dramatically enhanced at specific sizes call as "magic numbers". Photoionization mass spectra of sodium cluster $(Na)_n$ with small and large size regions are shown in Figs. 1.1 (a) and (c), respectively. The mass peaks at n = 8, 20, 40, 58 and 92 are more intense than those of the neighbors (Fig. 1.1 (a)), indicating that these magic clusters are more stable and produced more abundantly than the others.[2] The extraordinarily high stabilities of the Na clusters with these magic sizes are explained in terms of the closure of the electronic shells at 1p, 2s, 2p, 1g, and 1h (Fig. 1.1 (b)). On the other hand, the ion intensity distribution in the size region of n > 2000 (Fig. 1.1 (c)) exhibits local minima at n ~ 2820, 3800, 5070, and 6550, reflecting smaller ionization efficiency due to relatively larger ionization potentials at these sizes.[3] These magic clusters were assigned to the close-packed cuboctahedral and nearly close-packed icosahedral structures since these closed-shell clusters have relatively larger ionization potentials. Magic numbers found in other types of clusters such as ionic (*e.g.* alkali halide[4,5]) and van der Waals (*e.g.* rare gas[6]) clusters are also governed by geometric structures. Alkali halide clusters at magic compositions form cubic lattice of metal cations and halogen anions into cuboids such as 3×3×3 and 3×3×5. Rare gas clusters such as Xe_n form closed icosahedral shells at magic sizes of n = 13, 55 and 147.
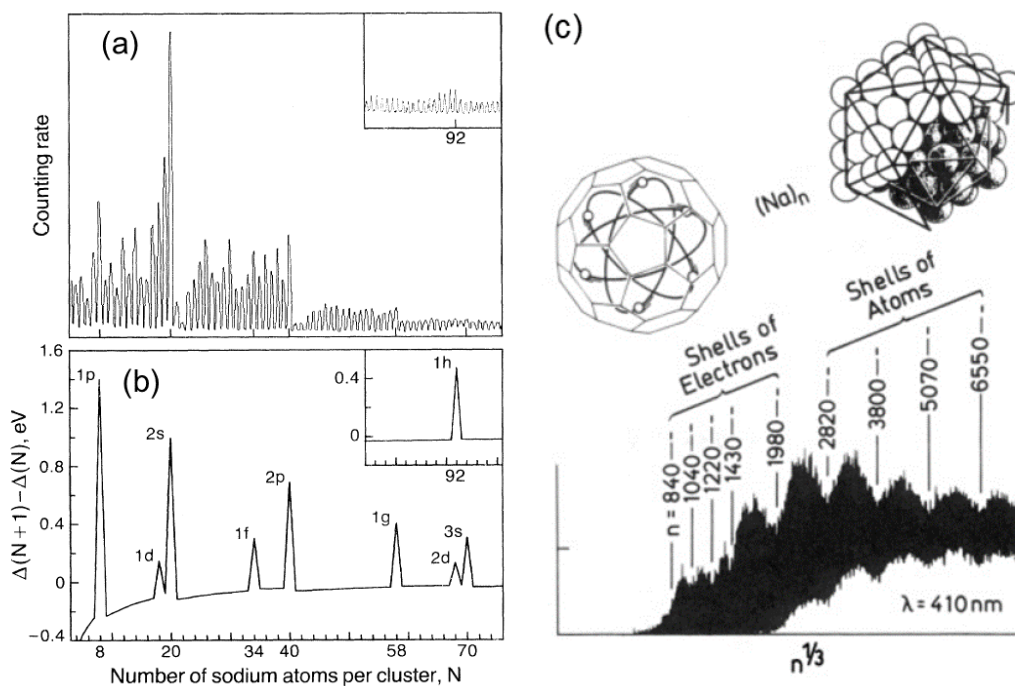
Figure 1.1. Mass spectra of (Na)$_n$ clusters in (a) small and (c) large size range. (b) The calculated change in the electronic energy difference. Reprinted with permission from ref. 2 for (a) and (b), Copyright 1984 American Physical Society. Reprinted with permission from ref. 3 for (c), Copyright 1991 American Chemical Society.

1.1.2. Reaction with oxygen

Chemical reactions of metal clusters toward oxygen molecule were investigated in the gas phase to gain a molecular-level insight into the mechanism of cluster-catalyzed oxidation reactions.[7–18] Inspired by the discovery of CO oxidation by nano-sized gold by Haruta,[19] the reactions of Au clusters and O$_2$ have been studied extensively. It was found that the reactivity of Au$_n^-$ toward O$_2$ showed drastic size dependence as shown in Fig. 1.2 (a): even-sized and magic-numbered (n = 8, 18, and 20) Au$_n^-$ exhibited significantly higher reactivity than the others.[7–9] The electron affinity of Au$_n$ also showed a similar size dependence: the electron affinities of even-sized and magic-numbered (n = 8, 18, 20, 34,
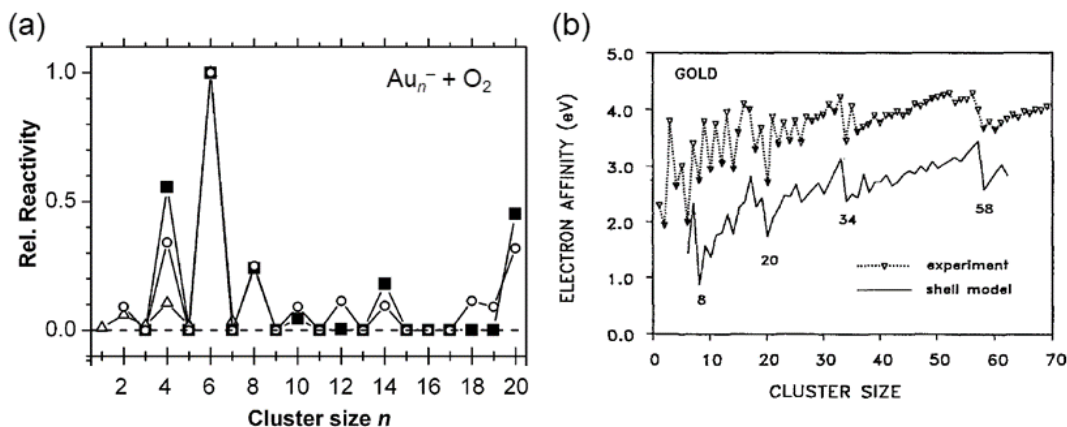
Figure 1.2. (a) Reactivity of Au_n^- toward O_2. (b) Electron affinities of Au_n clusters. Reprinted with permission from ref. 9 for (a), Copyright 2005 Elsevier. Reprinted with permission from ref. 10 for (b), Copyright 1992 AIP Publishing.

and 58) Au_n are smaller than those of the others as shown in Fig. 1.2 (b).[10] Good correlation between size-dependent reactivity and size-dependent electron affinity suggested that the electronic charge transfer is the key for this reaction. Namely, the Au_n^- clusters with $n = 2, 4, 6, 8, 10, 12, 14, 18$, and 20 undergo the reaction with O_2 via electron donation to the π_g^* anti-bonding orbital of O_2.

Not only the reactivity, but also adsorption motif of O_2 may change depending on the size of metal clusters. For example, photoelectron spectroscopy (PES) and theoretical calculation showed that Au_n^- with $n = 1, 3, 5$, and 7 form physisorbed complexes, while Au_n^- with $n = 2, 4, 6$, and 20 form chemisorbed complexes.[11–13] Molecular oxygen is chemisorbed to Au_n^- ($n = 2, 4, 6, 8$, and 20) in the superoxo (η^1) form, while it is chemisorbed to larger Au_n^- ($n \geq 8$) in the peroxo (η^2) form.[14] Two structural isomers coexist at $n = 8$ and structural transition from superoxo to peroxo occurs at $n = 8$ (Fig. 1.3). The O_2 adsorbates in the peroxo motif is expected to be more reactive than those in the superoxo motif because the O–O bonds of the former are longer than those in the latter.

4
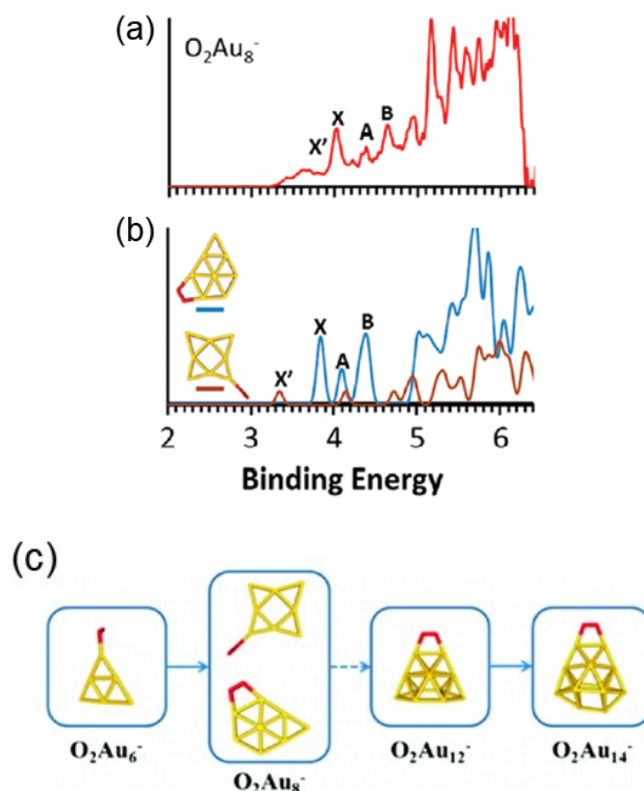
Figure 1.3. (a) Experimental and (b) computed PES spectra of $O_2Au_8^-$. (c) Schematic image of the size-dependence of the chemisorbed motif of O_2 on gold cluster anions. Reprinted with permission from ref. 14, Copyright 2012 American Chemical Society.

In contrast, the O_2 molecule undergoes dissociative adsorption of clusters of other transition metals such as Pt,[20] suggesting the different oxidation catalysis between Au and Pt clusters.

The O_2 chemisorbed on Au_n^- was applied for CO oxidation in the gas phase.[15–18] The Langmuir-Hinshelwood type reaction mechanism was proposed for CO oxidation by Au_6^- as shown in Fig. 1.4 (a).[15] The O_2 molecule and the CO molecule chemisorbed on the Au_6^- cluster undergo reaction, followed by desorption of CO_2. The remaining O atoms on Au_6^- is converted to CO_2 by another CO chemisorbed. On the other hand, it was demonstrated that small (<2 nm) clusters of transition metals stabilized by polymers
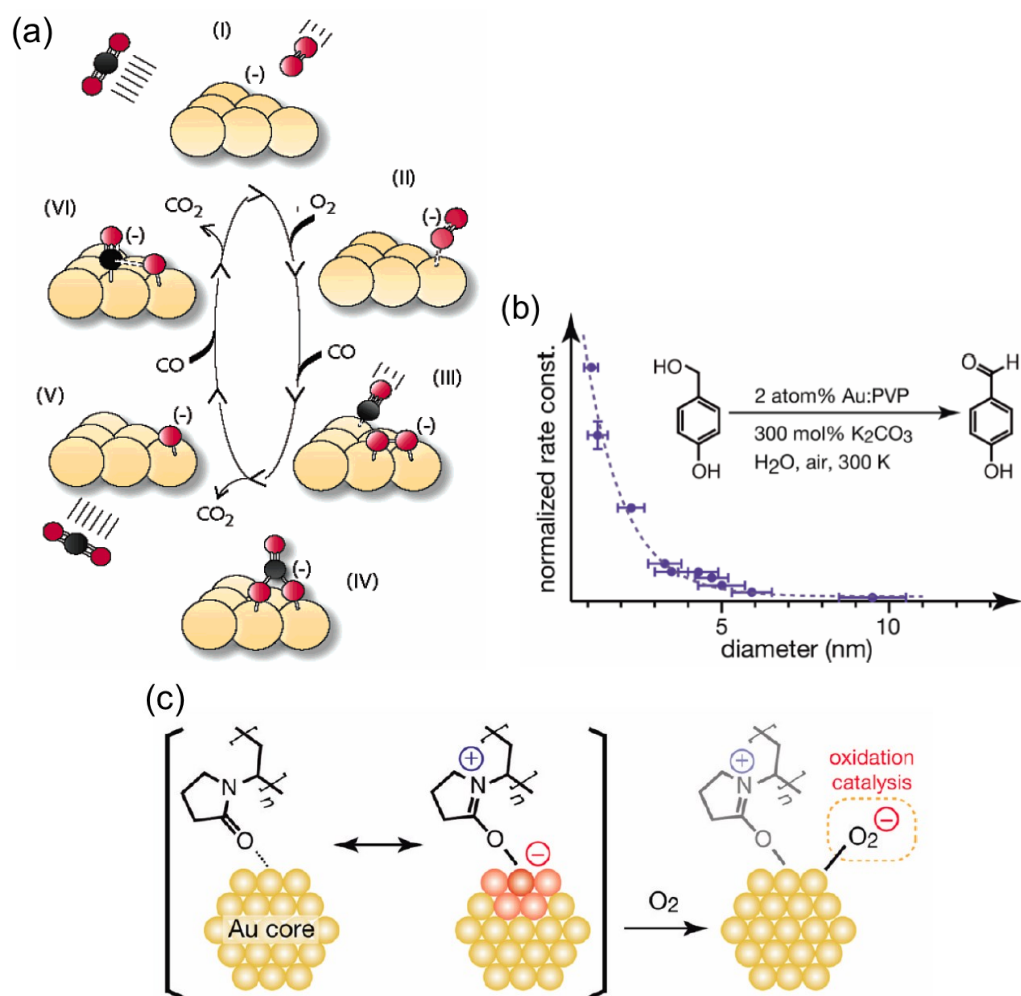
Figure 1.4. (a) Reaction mechanism of the CO oxidation catalyzed by Au_6^- cluster in the gas phase. (b) Dependence of catalytic activity on the size of Au:PVP for the oxidation of *p*-hydroxybenzyl alcohol. (c) Proposed mechanism of O_2 activation by Au:PVP. Reprinted with permission from ref. 15 for (a), Copyright 2002 American Chemical Society. Reprinted with permission from ref. 26 for (b) and (c), Copyright 2009 American Chemical Society.

catalyzed oxidation reactions under ambient conditions.[21–25] For example, the oxidation reactions of alcohols were catalyzed by sub-2-nm Au clusters stabilized by poly(*N*-vinyl-2-pyrrolidone) (PVP).[26] Remarkably, the catalysis of Au:PVP for aerobic oxidation was observed only when the cluster sizes are smaller than ~4 nm (Fig. 1.4 (b)). Vibrational spectroscopy on the adsorbed CO, X-ray photoelectron spectroscopy and X-ray absorption spectroscopy showed that the Au core of Au:PVP is negatively charged. On the basis of these spectroscopic studies, the reaction mechanism for aerobic oxidation by Au:PVP was proposed as shown in Fig. 1.4. (c). The Au cluster was negatively charged by the electron donation from PVP and the adsorbed O_2 molecule was activated by the electron transfer from the Au core. Electron transfer to oxygen was also supported by the density functional theory (DFT) calculation of Au_{13}(ethylpyrrolidone)$_4$ with O_2, in which ethylpyrrolidone represents a monomer unit of PVP.[27] These studies suggest that the key to the oxidation catalysis is reductive activation of O_2 by negatively charged Au clusters both isolated in the gas phase and stabilized by PVP. In summary, gas-phase studies of the reaction of molecules and metal clusters will provide useful insights into the catalytic activation mechanism of small molecules.

1.1.3. Sequential oxidation

When metal clusters are exposed to ambient conditions for practical application in catalysis, oxidation reaction may proceed sequentially. Since the oxidation reaction of metal clusters is generally an exothermic process, side reactions such as fragmentation may compete with the sequential oxidation reactions.[7,28–36] For example, the sequential oxidation of tantalum clusters led fragmentation into TaO and TaO_2.[36] Branching ratios between the oxidation and fragmentation pathway depended on the size of the metal

clusters. Small Ta_n^+ cluster cations ($n = 4$–8) gave fragments such as TaO under sequential

oxidations, while large Ta_n^+ cluster cations ($n = 13$–40) showed sequential addition of O_2

as a major pathway.[37] The branching ratio between the oxidation and fragmentation

depended also on the number of oxygen in $Ta_nO_m^+$. Upon the reaction with O_2, $Ta_4O_3^+$

and $Ta_4O_5^+$ selectively underwent the fragmentation and oxidation, respectively, whereas

$Ta_4O_4^+$ showed both reaction channels (Fig. 1.5). In addition to the reaction pathways, the

adsorption mode of oxygen may change depending on the degree of oxidation since the

structure of the adsorption sites may be changed in the course of sequential oxidations.

For example, O_2 is adsorbed dissociatively on $Ta_{20}(O_{2m})^+$ for $m \leq 7$, but molecularly for

$m > 7$ (Fig. 1.6).[37]
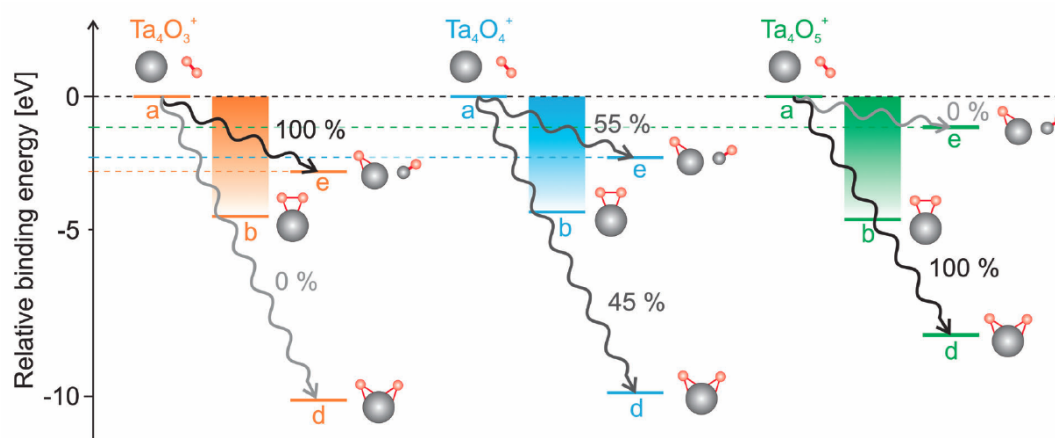
Figure 1.5. Potential energy diagram for species involved in the reaction of $Ta_4O_x^+$ ($x = 3$–5).
(a) $Ta_4O_x^+$ ($x = 3$–5). (b) The possible intermediate with chemisorbed oxygen, $Ta_4O_x(O_2)^+$. (d)
Intact oxidation product, $Ta_4O_{x+2}^+$. (e) Oxidative degradation product, $Ta_3O_{x+1}^+$. Reprinted with
permission from ref. 36, Copyright 2017 ROYAL SOCIETY OF CHEMISTRY; permission
conveyed through Copyright Clearance Center, Inc.
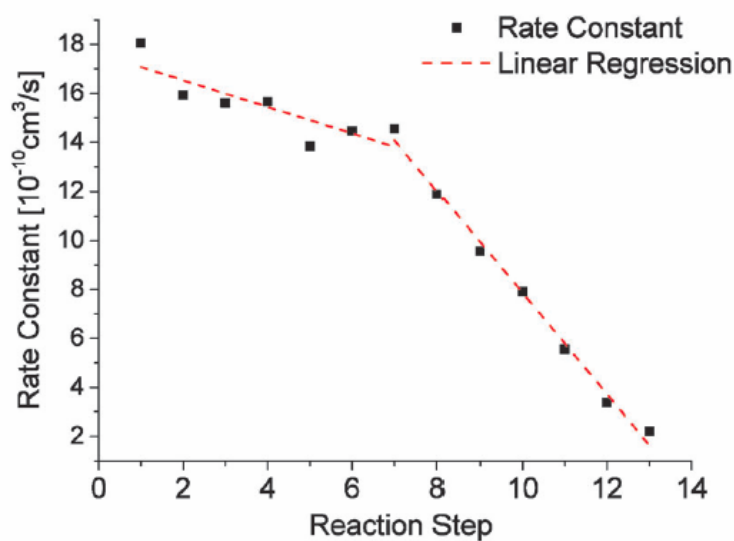
Figure 1.6. Rate constants for individual oxidation steps of Ta_{20}^+. The two dashed lines represent a linear regression for reaction steps 1–7 and 7–13 respectively, demonstrating the existence of two reaction regimes. Reprinted with permission from ref. 37, Copyright 2016 ROYAL SOCIETY OF CHEMISTRY; the Creative Commons Attribution 3.0 Unported License.

If the clusters do not show any activity to O_2, there is a possibility that the clusters can survive as stable species under ambient conditions. Most of the aluminum clusters were easily combusted by sequential oxidation by releasing AlO^-, AlO_2^- and Al_2O. However, the well-known magic clusters, Al_{13}^- and Al_{23}^-, were robust against oxidation due to its electronically closed shell structure with 40 and 70 valence electrons, respectively (Fig. 1.7 (a)).[38] In addition, the oxidation products such as $Al_{14}O^-$ and $Al_{15}O_2^-$ which have an icosahedral Au_{13}^- unit bonded by one or two AlO units were also stable against oxidation as shown in Fig. 1.7 (b).[39] Recently, the Al_{13}^- cluster was chemically synthesized using a dendrimer as a stabilizer.[40]
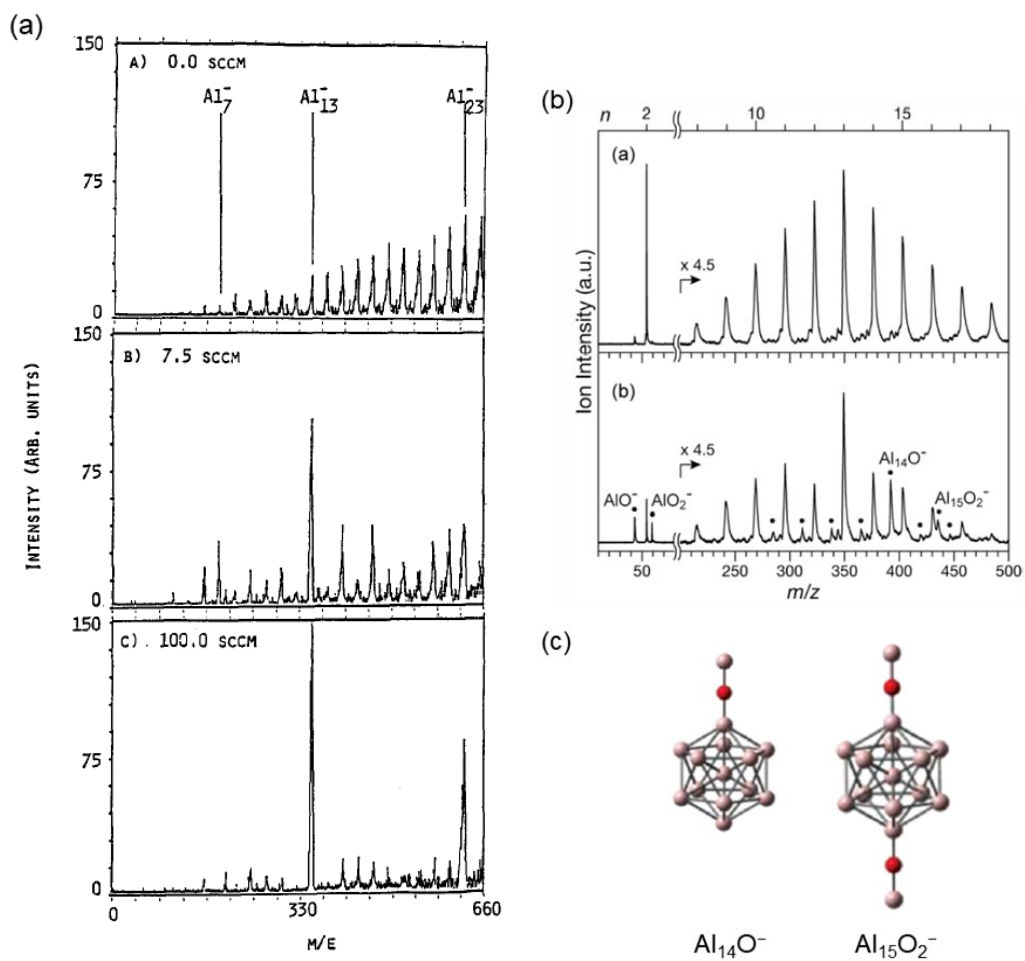
Figure 1.7. (a) (b) Mass spectra of Al_n^- reacted with oxygen under different condition. (c) Calculated structure of $Au_{14}O^-$ and $Au_{15}O_2^-$. Reprinted with permission from ref. 38 for (a), Copyright 1989 AIP Publishing. Reprinted with permission from ref. 39 for (b) and (c), Copyright 2013 American Chemical Society.

1.2. Aim and outline of the thesis

As mentioned in section 1.1, the study on the reaction of metal clusters toward O_2 provides the information about the catalytic oxidation reaction such as the reaction mechanism, intermediate species and activation process. Especially, metal oxide cluster can be viewed as the intermediate species in the catalytic oxidation reaction. The geometric structure, charge state and stoichiometry of the metal oxide clusters strongly influence their ability to transfer an oxygen atom to the reactant molecule.[41] The main purpose of this thesis is to reveal what kind of products are produced during the sequential oxidation of metal clusters. In particular, I focused on the early stage of the oxidation reaction in order to gain insights into the formation process of the metal oxide species in nanoscale. I investigated how oxygen atoms are bonded to the metal cluster and how the structure of the metal cluster is changed as the oxidation proceeds (Fig. 1.8).
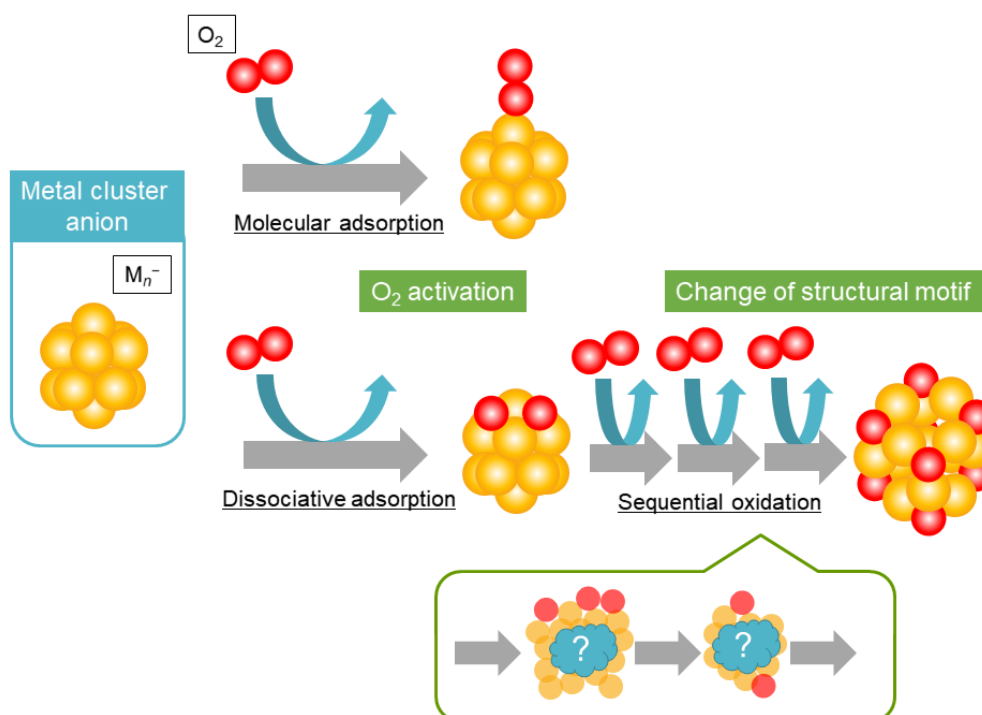
Figure 1.8. Schematic image of the purpose of this thesis.

In this thesis, group IX metals of cobalt and iridium were selected as the target elements. Co and Co oxide nanoparticles have gained much attention due to high abundance in natural resource and low price and their catalytic application have been studied for Fisher-Tropsch reaction, water splitting and oxidation reactions of alcohol and CO.[42–45] Ir and Ir oxide nanoparticles are potential candidates of novel catalysts because they exhibit remarkably different selectivity in hydrogenation from the conventional transition metal catalysts.[46–49] However, fundamental information of small Co and Ir clusters is limited. Previous theoretical studies[50–57] proposed that the structures of the Ir clusters and Co clusters were different although they are both group IX metals. In addition, the stable compositions of the oxide phase are different between Co and Ir. Ir has +4 oxidation state while Co has +2 or +3 state. Therefore, it is expected that the stable composition and structure of oxides were different.

Chapter 2 focuses on the stabilities and structures of Co oxide clusters. I discovered two types of magic Co oxide anions by mass spectrometry and studied their geometric and electronic structure by using PES combined with DFT calculation. The two types of magic compositions were attributed to the kinetic bottleneck at the surface oxidized stage in the sequential oxidation reactions and to the longer life time against the thermionic electron emission reaction.

Chapter 3 summarizes the structural evolution of the Ir oxide cluster anions. The composition and structure of iridium oxides were examined by the ion mobility mass spectrometry combined with theoretical calculations. It was found that the oxygen atoms were basically bonded to the terminal site of the Ir core as the on-top motif. In $Ir_8O_m^-$, structural transition from on-top motif on terminal site to μ_2 motif on bridge site occurred at $m = 11$. These results suggested that the Ir cluster core was retained in the oxidized

composition less than Ir:O~1:1 as increasing the number of oxygen atoms and further oxidation induced the core distortion and bonding motif transition.

Finally, chapter 4 concludes the thesis by discussing the difference between the Co and Ir oxide clusters. Future prospects are also given.

References

1. Mingos, D. M. P.; Wales, D. J. *Introduction to Cluster Chemistry*; Prentice-Hall International, Inc: London, 1990.

2. Knight, W. D.; Clemenger, K.; de Heer, W. A.; Saunders, W. A.; Chou, M. Y.; Cohen, M. L. *Phys. Rev. Lett.* **1984**, *52*, 2141.

3. Martin, T. P.; Bergmann, T.; Goehlich, H.; Lange, T. *J. Phys. Chem.* **1991**, *95*, 6421.

4. Mori, K.; Hiraoka, K. *Int. J. Mass Spectrom.* **2008**, *269*, 95.

5. Ohshimo, K.; Komukai, T.; Takahashi, T.; Norimasa, N.; Wu, J. W. J.; Moriyama, R.; Koyasu, K.; Misaizu, F. *Mass Spectrom.* **2014**, *3*, S0043.

6. Echt, O.; Sattler, K.; Recknagel, E. *Phys. Rev. Lett.* **1981**, *47*, 1121.

7. Lee, T. H.; Ervin, K. M. *J. Phys. Chem.* **1994**, *98*, 10023.

8. Salisbury, B. E.; Wallace, W. T.; Whetten, R. L. *Chem. Phys.* **2000**, *262*, 131.

9. Bernhardt, T. M. *Int. J. Mass Spectrom.* **2005**, *243*, 1.

10. Taylor, K. J.; Pettiette-Hall, C. L.; Cheshnovsky, O.; Smalley, R. E. *J. Chem. Phys.* **1992**, *96*, 3319.

11. Stolcic, D.; Fischer, M.; Ganteför, G.; Kim, Y. D.; Sun, Q.; Jena, P. *J. Am. Chem. Soc.* **2003**, *125*, 2848.

12. Kim, Y. D.; Fischer, M.; Ganteför, G. *Chem. Phys. Lett.* **2003**, *377*, 170.

13. Huang, W.; Zhai, H.-J.; Wang, L.-S. *J. Am. Chem. Soc.* **2010**, *132*, 4344.

14. Pal, R.; Wang, L. M.; Pei, Y.; Wang, L. S.; Zeng, X. C. *J. Am. Chem. Soc.* **2012**, *134*, 9438.

15. Wallace, W. T.; Whetten, R. L. *J. Am. Chem. Soc.* **2002**, *124*, 7499.

16. Hagen, J.; Socaciu, L. D.; Elijazyfer, M.; Heiz, U.; Bernhardt, T. M.; Wöste, L. *Phys. Chem. Chem. Phys.* **2002**, *4*, 1707.

17. Lopez, N.; Nørskov, J. K. *J. Am. Chem. Soc.* **2002**, *124*, 11262.

18. Johnson, G. E.; Reilly, N. M.; Tyo, E. C.; Castleman, A. W. *J. Phys. Chem. C* **2008**, *112*, 9730.

19. Haruta, M.; Kobayashi, T.; Sano, H.; Yamada, N. *Chem. Lett.* **1987**, 405.

20. Shi, Y.; Ervin, K. M. *J. Chem. Phys.* **1998**, *108*, 1757.

21. Tsunoyama, H.; Sakurai, H.; Negishi, Y.; Tsukuda, T. *J. Am. Chem. Soc.* **2005**, *127*, 9374.

22. Wang, T.; Shou, H.; Kou, Y.; Liu, H. *Green Chem.* **2009**, *11*, 562.

23. Tsukuda, T.; Tsunoyama, H.; Sakurai, H. *Chem. Asian J.* **2011**, *6*, 736.

24. Yamazoe, S.; Koyasu, K.; Tsukuda, T. *Acc. Chem. Res.* **2014**, *47*, 816.

25. Siyo, B.; Schneider, M.; Pohl, M. M.; Langer, P.; Steinfeldt, N. *Catal. Lett.* **2014**, *144*, 498.

26. Tsunoyama, H.; Ichikuni, N.; Sakurai, H.; Tsukuda, T. *J. Am. Chem. Soc.* **2009**, *131*, 7086.

27. Okumura, M.; Kitagawa, Y.; Kawakami, T.; Haruta, M. *Chem. Phys. Lett.* **2008**, *459*, 133.

28. Jarrold, M. F.; Bower, J. E. *J. Chem. Phys.* **1987**, *87*, 5728.

29. Radi, P. P.; von Helden, G.; Hsu, M. T.; Kemper, P. R.; Bowers, M. T. *Int. J. Mass Spectrom. Ion Process.* **1991**, *109*, 49.

30. Hintz, P. A.; Ervin, K. M. *J. Chem. Phys.* **1995**, *103*, 7897.

31. Griffin, J. B.; Armentrout, P. B. *J. Chem. Phys.* **1997**, *106*, 4448.

32. Griffin, J. B.; Armentrout, P. B. *J. Chem. Phys.* **1998**, *108*, 8062.

33. Engeser, M.; Weiske, T.; Schröder, D.; Schwarz, H. *J. Phys. Chem. A* **2003**, *107*, 2855.

34. Vardhan, D.; Liyanage, R.; Armentrout, P. B. *J. Chem. Phys.* **2003**, *119*, 4166.

35. Liu, F.; Li, F. X.; Armentrout, P. B. *J. Chem. Phys.* **2005**, *123*, 064304.

36. Eckhard, J. F.; Neuwirth, D.; Panosetti, C.; Oberhofer, H.; Reuter, K.; Tschurl, M.; Heiz, U. *Phys. Chem. Chem. Phys.* **2017**, *19*, 5985.

37. Neuwirth, D.; Eckhard, J. F.; Visser, B. R.; Tschurl, M.; Heiz, U. *Phys. Chem. Chem. Phys.* **2016**, *18*, 8115.

38. Leuchtner, R. E.; Harms, A. C.; Castleman, A. W. *J. Chem. Phys.* **1989**, *91*, 2753.

39. Watanabe, T.; Tsukuda, T. *J. Phys. Chem. C* **2013**, *117*, 6664.

40. Kambe, T.; Haruta, N.; Imaoka, T.; Yamamoto, K. *Nat. Commun.* **2017**, *8*, 2046.

41. Zemski, K. A.; Justes, D. R.; Castleman, A. W. *J. Phys. Chem. A* **2001**, *105*, 10237.

42. Kang, M.; Song, M. W.; Lee, C. H. *Appl. Catal. A* **2003**, *251*, 143.

43. Khodakov, A. Y.; Chu, W.; Fongarland, P. *Chem. Rev.* **2007**, *107*, 1692.

44. Zhu, J.; Kailasam, K.; Fischer, A.; Thomas, A. *ACS Catal.* **2011**, *1*, 342.

45. Liao, L.; Zhang, Q.; Su, Z.; Zhao, Z.; Wang, Y.; Li, Y.; Lu, X.; Wei, D.; Feng, G.; Yu, Q.; Cai, X.; Zhao, J.; Ren, Z.; Fang, H.; Robles-Hernandez, F.; Baldelli, S.; Bao, J. *Nat. Nanotechnol.* **2014**, *9*, 69.

46. Tamura, M.; Tokonami, K.; Nakagawa, Y.; Tomishige, K. *Chem. Commun.* **2013**, *49*, 7034.

47. Sharif, M. J.; Maity, P.; Yamazoe, S.; Tsukuda, T. *Chem. Lett.* **2013**, *42*, 1023.

48. Tamura, M.; Tokonami, K.; Nakagawa, Y.; Tomishige, K. *ACS Catal.* **2016**, *6*, 3600.

49. Higaki, T.; Kitazawa, H.; Yamazoe, S.; Tsukuda, T. *Nanoscale* **2016**, *8*, 11371.

50. Fan, H.-J.; Liu, C.-W.; Liao, M.-S. *Chem. Phys. Lett.* **1997**, *273*, 353.

51. Zhang, W.; Xiao, L.; Hirata, Y.; Pawluk, T.; Wang, L. *Chem. Phys. Lett.* **2004**, *383*, 67.

52. Pawluk, T.; Hirata, Y.; Wang, L. *J. Phys. Chem. B* **2005**, *109*, 20817.

53. Datta, S.; Kabir, M.; Ganguly, S.; Sanyal, B.; Saha-Dasgupta, T.; Mookerjee, A. *Phys. Rev. B* **2007**, *76*, 014429.

54. Sebetci, A. *Chem. Phys.* **2008**, *354*, 196.

55. Du, J.; Sun, X.; Chen, J.; Jiang, G. *J. Phys. Chem. A* **2010**, *114*, 12825.

56. Chen, Y.; Huo, M.; Chen, T.; Li, Q.; Sun, Z.; Song, L. *Phys. Chem. Chem. Phys.* **2015**, *17*, 1680.

57. Jorge, F. E.; Venancio, J. R. da C. *Chin. Phys. B* **2018**, *27*, 063102.

Chapter 2.

Oxidation reaction of cobalt clusters

2.1. Introduction

Nanoparticles of metallic cobalt and its oxide are expected to be key building units of functional materials such as Li-ion batteries, magnetic materials, and catalysts.[1–3] To improve the functionalities and to optimize the performance of Co/CoO nanocomposites, much effort has been expended to control their structures. As a result, several methods have been developed to tune the diameter of the Co core and thickness of the CoO shell. An interesting example includes the production of hollow CoO nanocrystals via the Kirkendall effect by rapid diffusion of Co atoms through the oxide layer.[4,5]

Geometrical structures and chemical properties of sub-nanometer sized clusters of cobalt oxide ($Co_nO_m^{\pm/0}$) are significantly different from those of the bulk (CoO and Co_3O_4) and vary dramatically depending on the compositions and charge states.[6–17] Mass analysis of $Co_nO_m^{\pm/0}$ produced by laser vaporization of a Co_3O_4 target[6,7] or a Co rod in the presence of O_2[8–13] showed that the compositions with $m = n$ and $n+1$ are preferred. Although these compositions are comparable to that in the bulk (CoO), their structures are significantly different. A cubane and a planar structures were proposed for $Co_4O_4^-$[7] and $Co_4O_4^+$,[12–15] respectively. Tower structures based on a ring Co_3O_3 or a cage structure were proposed for Co_nO_n ($n = 3, 4, 6, 9, 12$).[9] Under certain conditions, oxygen-deficient clusters such as $Co_9O_6^+$ and $Co_{13}O_8^+$ were observed abundantly.[16] It was predicted that six O atoms cap the triangle facets of a tri-capped trigonal Co_9 prism in $Co_9O_6^+$ and that eight O atoms occupy (111) facets of cuboctahedral Co_{13} in $Co_{13}O_8^+$.[17]

In contrast to the structural information, much less is known about the mechanism of oxidation of Co clusters. Previous report showed that the production of $Co_nO_m^-$ ($n = 1$, 2) via $Co_x^- + O_2$ ($x = 2–7$) involves extensive fragmentation.[18] The aim of this study is to gain atomistic insights into the early stage of oxidation process of the anionic form of Co

clusters, Co_n^- ($n \leq 10$). To this end, we monitored the anomalies in the abundance distributions of $Co_nO_m^-$ produced in the reaction of Co_n^- and O_2 with a varied pressure since observation of magic compositions provides information on kinetic bottleneck for further oxidation, dissociation into smaller fragments, or thermionic emission. Population analysis of $Co_nO_m^-$ with each n as a function of the number of O atoms revealed two types of magic compositions: the population dropped abruptly by removing one O atom from or by adding one O atom to magic composition. On the basis of photoelectron spectroscopy, magic compositions of the former type were ascribed to the retardation of thermionic emission from $Co_nO_m^-$ during the relaxation. There were two series in the latter type of magic compositions with the n:m ratio of ~3:4 and ~1:1. DFT calculations on $Co_7O_m^-$ ($m = 0$, 3–6) and $Co_6O_m^-$ ($m = 0$, 5) illustrated that the O atoms were sequentially bonded to the surface of the Co core while retaining its geometry in the early stage of the oxidation ($m < n$). These results suggested that magic compositions with n:m ~ 3:4 and ~ 1:1 correspond to the fully oxidized states and surface oxidized states, respectively. The origin of the kinetic bottleneck at n:m ~ 1:1 is associated with significant structural change of the Co_n moiety required for the internal oxidation.

2.2. Methods

2.2.1. Mass spectrometry and photoelectron spectroscopy (PES)

2.2.1.1. Principles of operation

Mass spectrometry is the powerful method to get information on the composition of the target ion. In fact, mass spectrometry played a key role to determine the composition of the product clusters in this experiments. There are several types of mass spectrometer such as magnetic sector, quadrupole, time-of-flight, and so on. In this study, time-of-flight

mass spectrometer (TOF-MS) was adopted because the mass range of TOF-MS is unlimited in principle. The mass of metal clusters is relatively heavy compared to that of small organic molecules which is typically analyzed by quadrupole mass spectrometer.

In the case of TOF-MS, the TOF from acceleration to detection of ions were measured and TOF is converted to m/z value, which is defined as the dimensionless quantity formed by dividing the ratio of the mass of an ion to the unified atomic mass unit by its charge number (regardless of sign)[19]. In the apparatus used in this study, ions were first introduced to acceleration region, then extracted perpendicularly by pulsed high voltage in order to remove the contaminated neutral species and oppositely charged ions to target ion and finally detected by a detector as shown in Fig. 2.1.
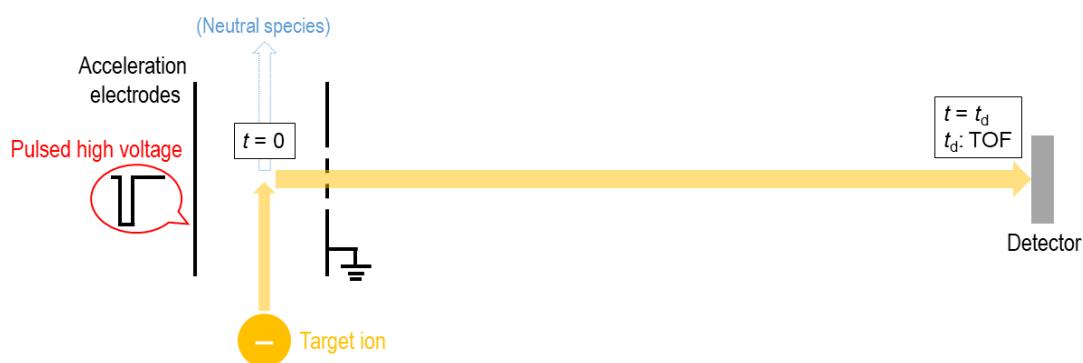
Figure 2.1. Schematic image of the TOF-MS.

In order to improve the resolution of the mass and efficiency of the detection, Wiley-McLaren type acceleration system,[20] deflector and einzel lens are installed in the apparatus. In principle, the relationship between TOF and m/z can be written as the eq. (2.1).

$$\text{TOF} \propto \sqrt{m/z} \tag{2.1}$$

Practically, the coefficients *a* and *b* in the calibration equation written as eq. (2.2) were determined by using a least-squares fitting of the calculated *m/z* values and experimental TOF values of the standard species.[21–23]

$$\text{TOF} = a\sqrt{m/z} + b \tag{2.2}$$

PES gives us the information on electronic structure of the target anions. In the experiment, electron binding energy (EBE) can be obtained by measuring kinetic energy (KE) of the electron (Fig. 2.2). In this study, first the laser was shined to target molecule to kick out an electron, then ejected electron was extracted to the flight tube and finally the electron was detected. TOF of electron was measured and converted to the KE by using the relationship of TOF and KE written as eq. (2.3). Obtained KE was converted to EBE by using eq. (2.4). In the experiment, the calibration eq. (2.5) was first derived by applying least-square method to the eq. (2.5) between the reported value of EBE in literature and experimental TOF value of standard species.

$$\text{KE} \propto \frac{1}{TOF^2} \tag{2.3}$$

$$\text{EBE} = h\nu - \text{KE} \tag{2.4}$$

$$\text{TOF} = a\sqrt{1/KE} + b \tag{2.5}$$
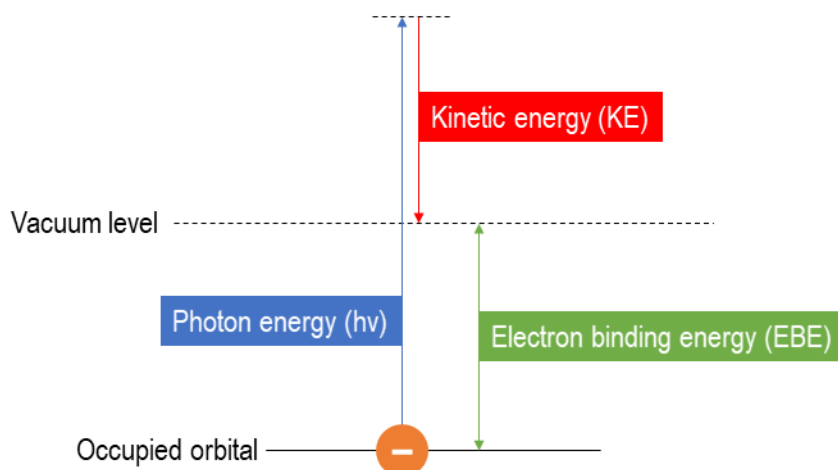
Figure 2.2. Schematic image of the photoelectron spectroscopy.

In addition, Jacobian has to be considered to the intensity during conversion of TOF to energy as eq (2.6).[24]

$$I(t)dt = J(\varepsilon)t^3 d\varepsilon \qquad (2.6)$$

(I, J: intensity, t: TOF, ε: energy)

From obtained photoelectron spectra, we can determine the vertical detachment energy (VDE) as the top of the peak assigned to the each transition. VDE is the energy difference between ground state of anion and the state of neutral whose structure is same as that of anion as shown in Fig. 2.3. In addition, when the structure of anion and neutral species are similar, adiabatic electron affinity (AEA) can be obtained as the rising edge of the first peak. AEA is the energy difference between ground state of anion and ground state of neutral. In the case of atomic anions, VDE is in accordance with AEA because the structures of anion and neutral are completely same and the atomic lines can be obtained as the spectrum.
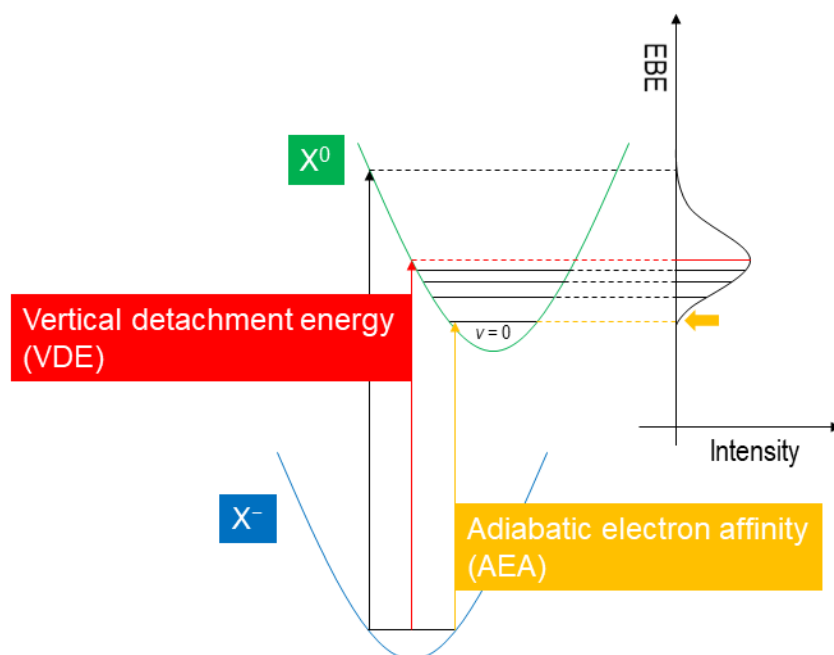
Figure 2.3. Schematic image of VDE and AEA.

2.2.1.2. Experimental setup

Experiments were performed using a home-made apparatus[25–27] composed of a cluster source, reaction cell, TOF-MS, and magnetic-bottle photoelectron spectrometer (MB-PES) as shown in Fig. 2.4. Neutral and ionized Co clusters were generated by the irradiation of the focused output of the second harmonic of a Nd:YAG laser (532 nm, Spectra-Physics, INDI-HG) with typical pulse energy of 100–200 mJ/pulse by repetition rate of 10 Hz on a rotating and translating cobalt rod (99.98%; φ = 5 mm; L = 18 mm) under a pulsed helium carrier gas (99.999 %) with backing pressure of 0.6–0.9 MPa through a pulse valve (Parker Hannifin, series 9, injection orifice: 0.8 mm, pulse width ~300 μs). The Co clusters were introduced into a reaction cell filled with oxygen ($\geq$ 99.6 vol%) through another pulse valve. Finally, the anionic species were extracted perpendicularly to the initial beam by applying a pulsed high voltage (−3 kV, DEI, PVX-
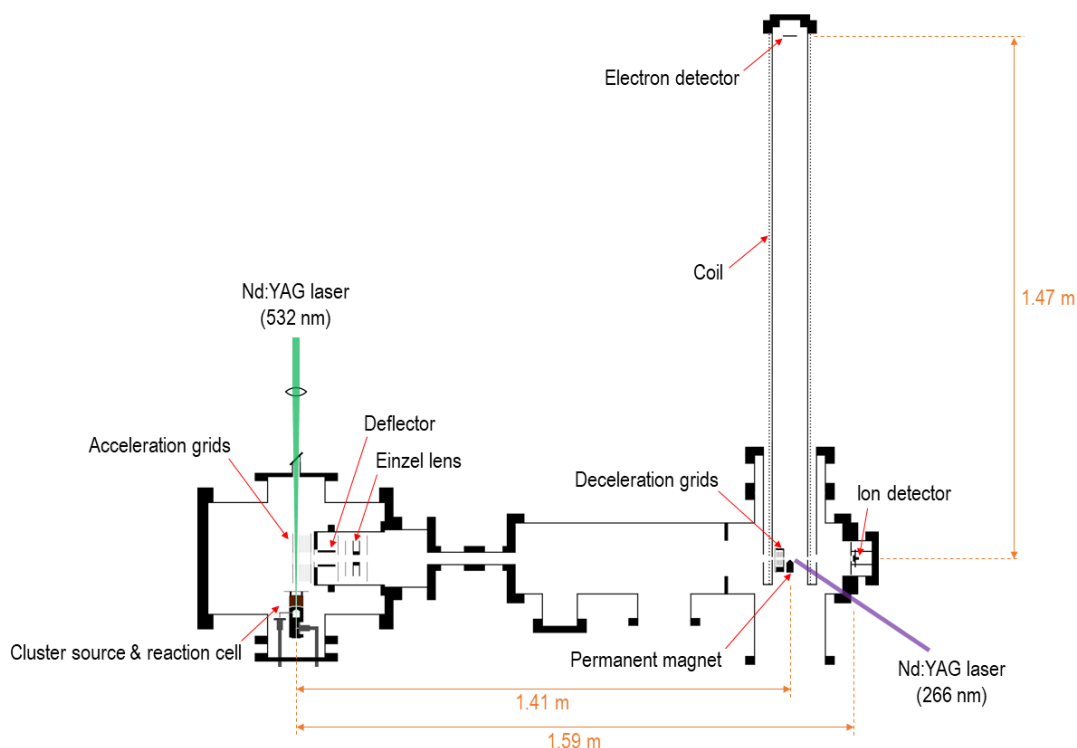
Figure 2.4. Schematic image of the experimental apparatus.

4140, pulse duration: 10 μs, pulse rise time: ~50 ns) into the TOF-MS with a flight path of 1.59 m. Acceleration grids are composed of repeller grid, extractor grids and ground electrode (Fig. 2.5). Extractor grids and ground electrode are connected by resistors. This Wiley-McLaren type acceleration grids can focus the ions at the detector by adjusting applied voltage. In this experiment, the voltage applied to extractor (V_{Ext}) was optimized to get high intensity of the target ions and typical value of V_{Ext} was 2.7 kV. In order to enhance the efficiency of the detection, the trajectory of the flying ions were modified by deflectors and einzel lens. Typically ~70 V and −1.00 kV were applied to horizontal deflector and einzel lens, respectively, by using DC power supply (KENWOOD, PA500-0.1A; Matsusada). Finally, product anions were detected by a microchannel plate (Hamamatsu Photonics, F4655-12). The signals were recorded and accumulated by a
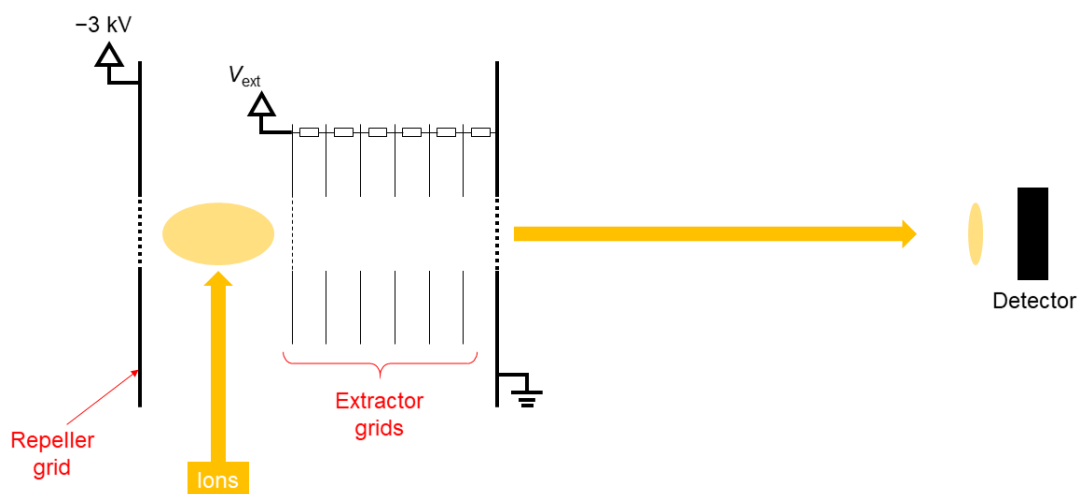
Figure 2.5. Schematic image of the acceleration grids.

digital oscilloscope (Tectronix, TDS580D) for typically 3000–10000 laser shots. Resolution of the TOF-MS was ~400 at $m/z = 200$. In this experiment, mass spectra were calibrated by the series of bare cobalt cluster anions, Co_n^- shown in following section. Cobalt has only one stable isotope ^{59}Co so the peak shape of the mass spectra of Co_n^- was relatively narrow.

PES measurement was conducted by using MB-PES. The product anions were irradiated by the fourth harmonic of a Nd:YAG laser (266 nm, Spectra-Physics, INDI-40-TB-W) with ~5 mJ/pulse at the 1.41 m from acceleration center in the flight path. The laser was polarized horizontally. The detached photoelectrons were collected by an inhomogeneous magnetic field produced by a cylindrical permanent magnet (~1000 G) and a solenoid coil (~40 G, number of turns: ~670 m^{-1}, current: 5.2 A). The photoelectrons were detected after flight of 1.47 m by a microchannel plate (Hamamatsu Photonics, F1552-21S). The signals were amplified 5-fold by a preamplifier (Stanford Research Systems, SR445A) and counted by a multichannel scalar (Stanford Research

Systems, SR430). The spectra presented in this thesis were obtained by accumulating 5000–20000 laser shots and averaging the data of 10 points. The resolution of our MB-PES was 120 meV at the maximum for electrons with a kinetic energy of 1.0 eV. Photoelectron spectra were calibrated using those of I^- and Co_3^- after subtraction of background signals by comparing them with literature (VDE value; I^-: 3.0591 and 4.00178 eV,[28] Co_3^-: 1.66 eV[29]). During the acquisition of calibration data, magnitude of acceleration voltage was set to ~-1.6 kV and ions were decelerated by a pulsed electric field ($0–1.75\times10^5$ Vm^{-1}, pulse duration: 300 ns, Behlke, HTS 151-03-GSM) at 19 mm upstream from photodetachment region in order to get sharper peak by reducing the Doppler effect. Adiabatic electron affinity (AEA) of Co_nO_m was estimated by the onset of the photoelectron spectrum.[27,29–32] In this work, the spectral onset was defined as the electron binding energy at which the spectrum exhibits the largest curvature. Practically, AEA was determined to be the energy at which the second derivative of the spectrum took a local maximum because curvature ($\kappa(x)$) can be written as eq. (2.7) when the spectrum is written as $f(x)$ and it can be approximated as eq. (2.8) when $f'(x) \ll 1$.

$$\kappa(x) \ = \ \frac{f''(x)}{(1 + (f'(x))^2)^{\frac{3}{2}}} \qquad (2.7)$$

$$\kappa(x) \ \sim \ f''(x) \qquad (2.8)$$

During the experiment, all the pulse sequence were controlled by digital delay generators (Stanford Research Systems, DG645). Typical timing chart is shown in Fig. 2.6.
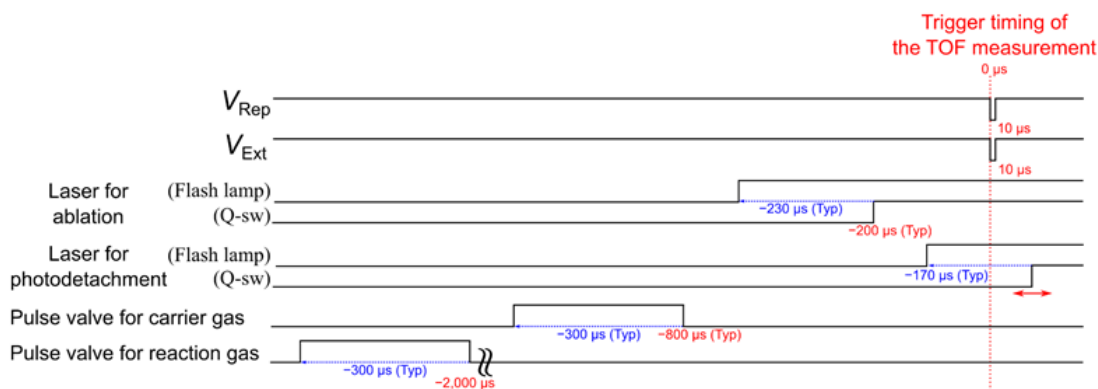
Figure 2.6. Schematic image of typical timing chart of the experiment.

In this setup, measurement of the pressure in reaction cell by using common vacuum gauge such as Pirani gauge and Baratron gauge was difficult because the pressure was changed rapidly. In addition, it was assumed that the pressure in reaction cell reached equilibrium with certain time-delay after the trigger signal to pulse valve. In order to know the pressure in reaction cell and the time-delay after trigger signal, I used the piezoelectric pressure sensor 601C manufactured by Kistler, whose rising time is less than 1.4 μs. This sensor gives us the information about relative pressure from the standard pressure which we can set freely (in this measurement, standard pressure is vacuum). Figs. 2.7 and 2.8 show the pressure change during the experimental condition depending on the opening time of pulse valve and back pressure of reaction gas, respectively, when the pulse valve opened at −2000 μ s from the acceleration (0 s). As shown in figures, pressure reached equilibrium at around −500 μs, which is enough early than laser irradiation timing (typically −200 μs). According to the results, the order of typical pressure was thought to be ~10^3 Pa or less so the order of the maximum number of collisions was expected to be ~10^5 collisions in the reaction cell.

27
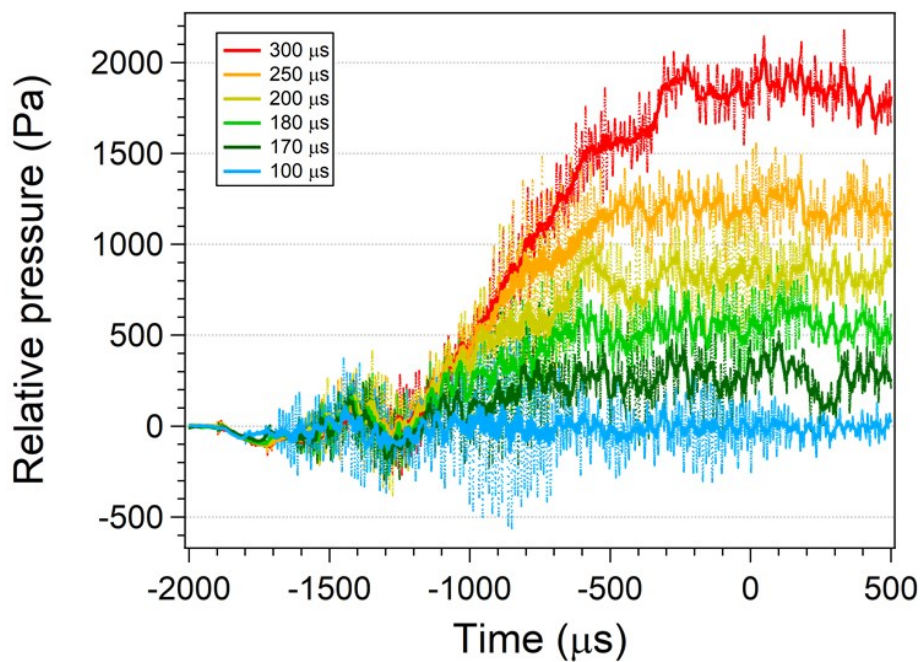
Figure 2.7. The dependence of opening time of pulse valve on the pressure in reaction cell. Back pressure of reaction gas was 1.1 MPa. Dots are raw data and solid lines are smoothed data by averaging 100pts.
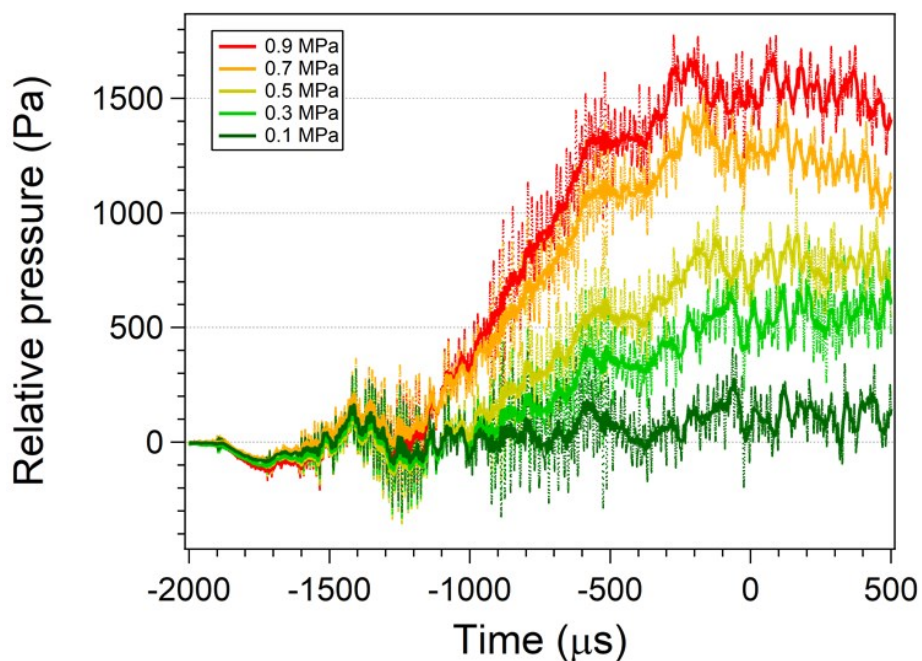
Figure 2.8. The dependence of back pressure of reaction gas on the pressure in reaction cell. Opening time of pulse valve was 300 μs. Dots are raw data and solid lines are smoothed data by averaging 100pts.

### 2.2.2. Theoretical calculations

The geometric and electronic structures of $Co_n^{-/0}$ and $Co_nO_m^{-/0}$ were investigated by the DFT calculation at the B3LYP/6-31+G(d) level. The spin multiplicities were surveyed in the range of 11–17 based on previous reports.[14,27] Vibrational frequencies were also calculated to confirm that the optimized structures correspond to local minimum structures. In the calculation of the relative energies, the zero-point energy was considered. The VDE was calculated by subtracting the energy of the most stable anion from that of the neutral state with the same structure as the anionic state without considering zero-point energy.[33] The AEA value was obtained by the energy difference between the optimized anion and the optimized neutral species. In the calculations of the VDEs and AEAs, we selected more stable species between those whose spin multiplicities differ from that of the anion by ±1 as the neutral clusters. The charge on each atom was estimated by using natural population analysis. All calculations were carried out using the Gaussian 09 program,[34] including NBO.[35] The results were visualized using PyMOL.[36]

2.3. Results

2.3.1. Magic compositions of $Co_nO_m^-$

The typical mass spectrum of Co_n^- before reaction with O_2 is shown in Fig. 2.9 (a). The Co_n^- clusters exhibited a smooth distribution with a small dip at $n = 6$, consistent with previous reports.[27,30,31] In the mass spectra, small peaks assigned to Co_nO^- and Co_nOH^- were also observed in addition to Co_n^-. The generation of the Co_nO^- and Co_nOH^- impurities was significantly suppressed by baking the stainless tubes used for gas supply, suggesting that the source of the oxygen for these impurities was residual water inside the tube.
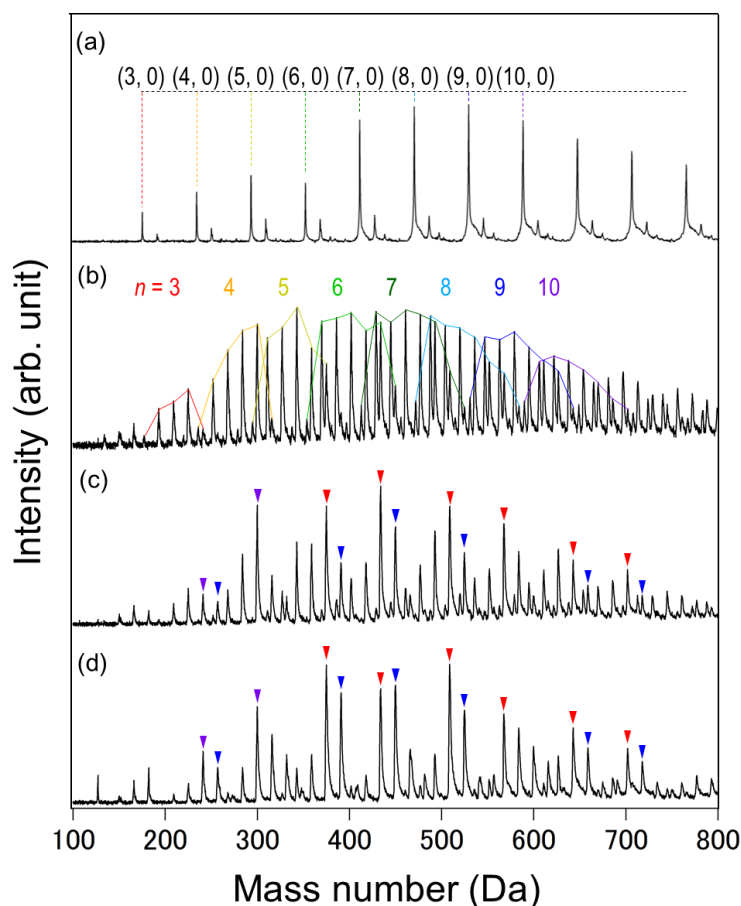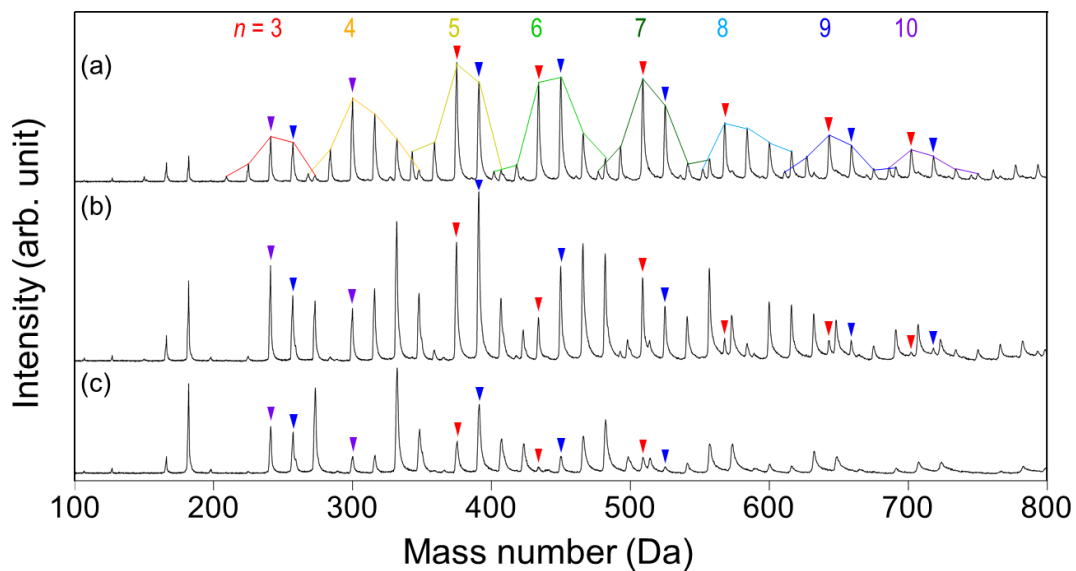
Figure 2.9. Mass spectra obtained at P_{O2} = 0.11 MPa with t_{PV} = (a) 0, (b) 140, (c) 150, (d) 200 µs. The notation (n, m) represents the chemical compositions of $Co_nO_m^-$. Red and blue triangles indicate the magic compositions of type **D** and **U**, respectively, whereas purple triangles represent those whose type cannot be assigned unambiguously. See text for the definitions of type **U** and **D** (P. 34).

The mass spectra were recorded while controlling the back pressure of the O_2 gas (P_{O2}) in the range of 0.11–0.30 MPa and the opening times of the pulse valve (t_{PV}) in the range of 140–900 µs. Fig. 2.9 (b)–(d) show typical mass spectra measured at P_{O2} = 0.11 MPa and t_{PV} = 140, 150, 200 µs, respectively. Fig. 2.10 and Fig. 2.11 show typical mass spectra measured at P_{O2} = 0.14 MPa and 0.30 MPa, respectively, and t_{PV} = 150, 400, 900 µs. Products with the formula $Co_nO_m^-$ (n = 2–13, m = 0–11) were observed. The
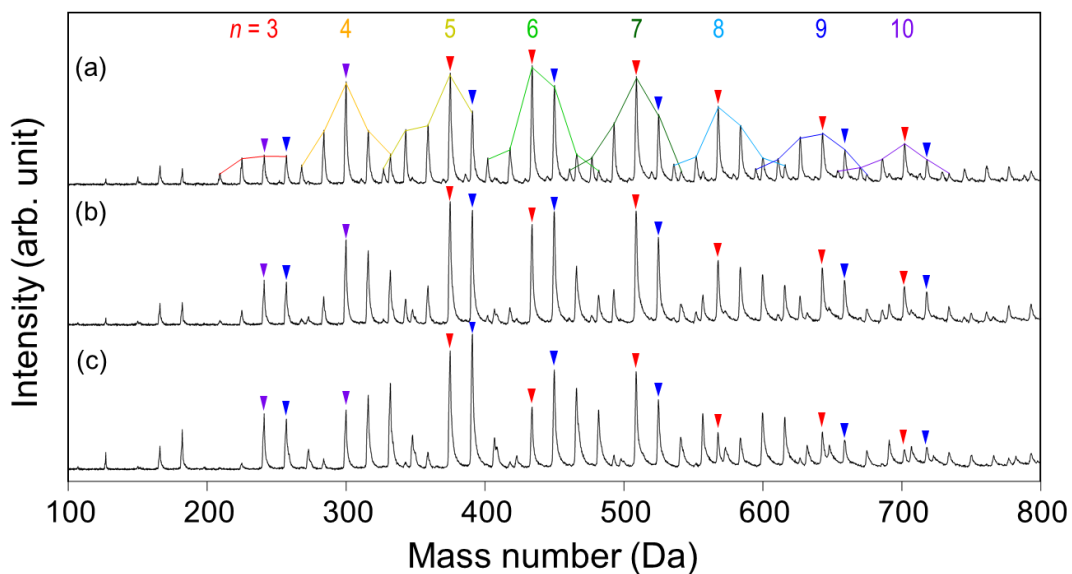
Figure 2.10. Mass spectra obtained at $P_{O2} = 0.14$ MPa and t_{PV} of (a) 150, (b) 400, and (c) 900 µs. Red and blue triangles indicate the magic compositions of type **D** and **U**, respectively, whereas purple triangles represent those whose type cannot be assigned unambiguously.

Figure 2.11. Mass spectra obtained at $P_{O2} = 0.30$ MPa and t_{PV} of (a) 150, (b) 400, and (c) 900 µs. Red and blue triangles indicate the magic compositions of type **D** and **U**, respectively, whereas purple triangles represent those whose type cannot be assigned unambiguously.

observation of large $Co_nO_m^-$ clusters with $n = 3\text{–}13$ was in sharp contrast to that of small $Co_nO_m^-$ with $n = 1$ and 2 in the previous report.[18] Observation of larger $Co_nO_m^-$ is due to the employment of larger Co_n^- clusters as reactants and efficient collisional cooling by He of the oxidizing clusters. In order to understand how the number distributions of O atoms (m) of $Co_nO_m^-$ change with the increase of O_2 concentration, the population $P_n(m)$ is defined as follows,

$$P_n(m) = I_{n,m} \Big/ \sum_m I_{n,m} \qquad (2.9)$$

where $I_{n,m}$ represents the peak intensities of $Co_nO_m^-$. $P_n(m)$ values were calculated from the mass spectra recorded under different conditions of t_{PV} and P_{O2} (Figs. 2.9–11) and plotted as a function of m in Fig. 2.12.

The distributions of $P_n(m)$ do not show any even-odd alternation with respect to m. This indicated that O_2 molecules underwent dissociative adsorption onto Co_n^-. The distribution of $P_n(m)$ was shifted to higher m values with increase of the t_{PV} and P_{O2} values, indicating the further oxidation proceeded with increase in O_2 concentration. In order to understand how the number distributions of Co atoms (n) of $Co_nO_m^-$ change with the increase of O_2 concentration, the population $P(n)$ is defined as follows,

$$P(n) = \sum_m I_{n,m} \Big/ \sum_n \sum_m I_{n,m} \qquad (2.10)$$

where the summation range for n is limited from 2 to 23 in this experiment because the ion intensities of other sizes were negligibly small. $P(n)$ values were obtained from
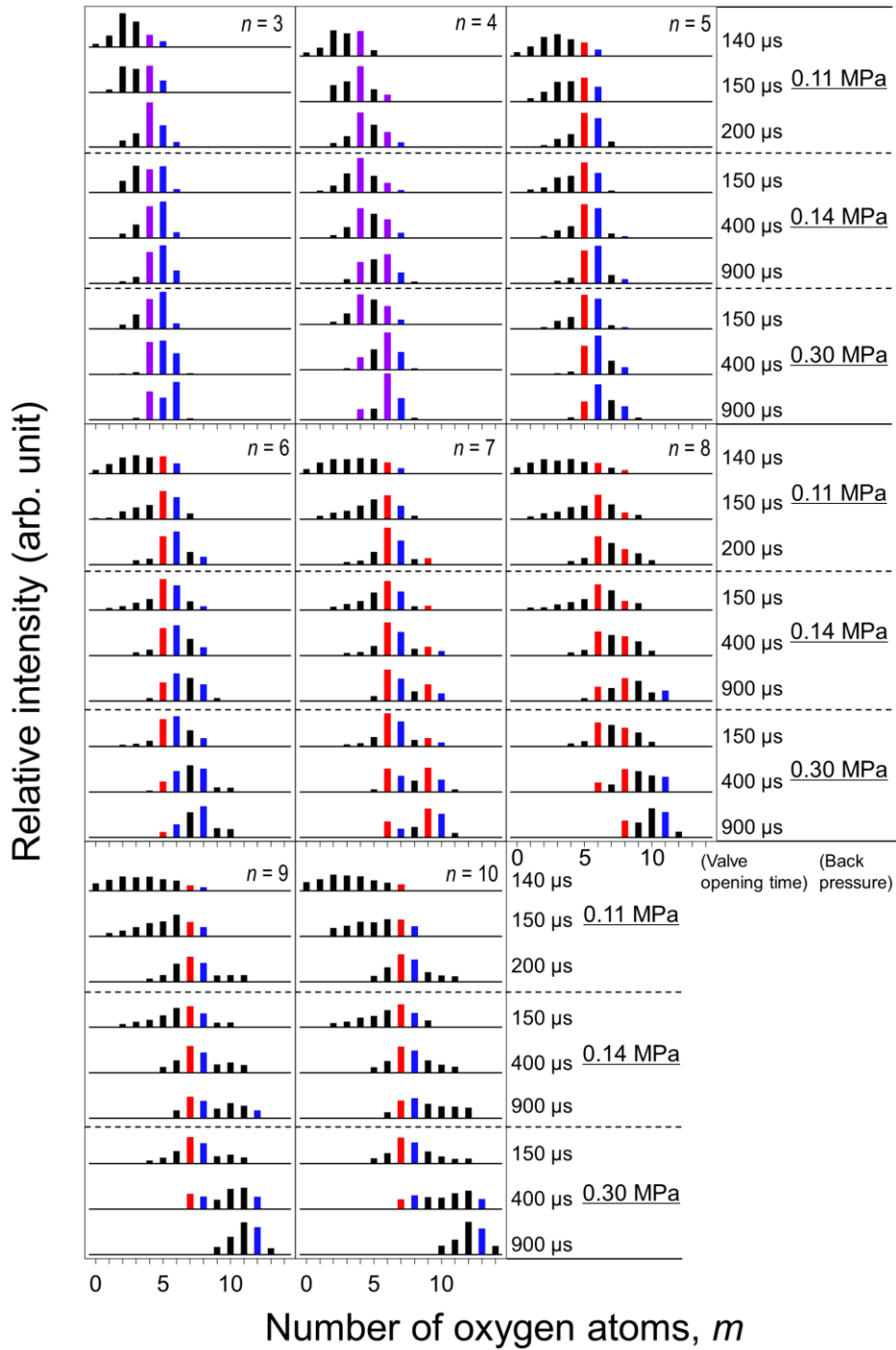
Figure 2.12. Distributions of $P_n(m)$ ($n = 3$–10, $m = 0$–14). Red and blue bars indicate the magic compositions of type **D** and **U**, respectively, whereas purple bars represent those whose type cannot be assigned unambiguously. See text for the definitions of type **U** and **D**.

the mass spectra recorded at $P_{O2} = 0.11$ MPa and different t_{PV} values (Fig. 2.9) and plotted as a function of n in Fig. 2.13. The distribution of $P(n)$ was shifted to smaller n with increase in the O_2 concentration. This trend clearly indicated that Co-containing species were released from internally-hot $[Co_xO_y]^{-*}$ clusters nascently formed via highly exothermic oxidation reaction.[18]
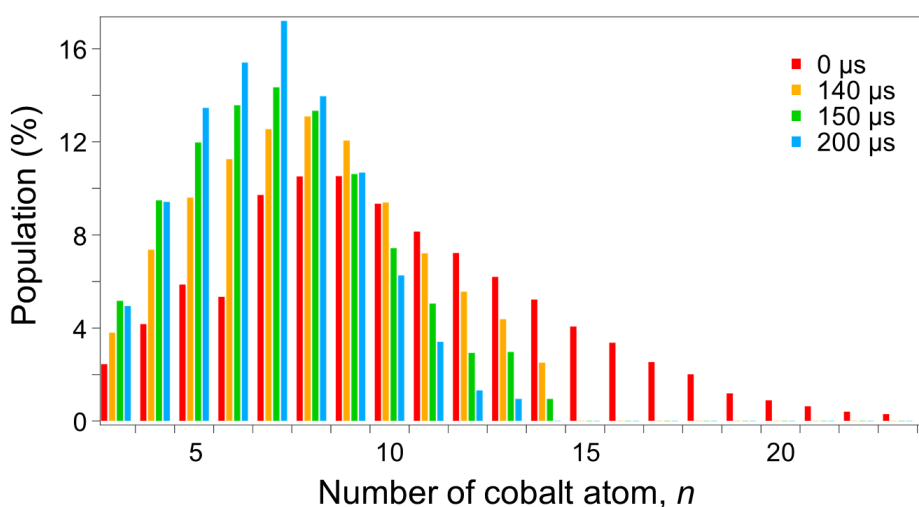

Figure 2.13. Distributions of $P(n)$ (n =3–10) at P_{O2} = 0.11 MPa.

Although the $P_n(m)$ distributions at low O_2 concentration appear to be smooth, clear discontinuities emerged at high O_2 concentration (Fig. 2.12). There are two types of discontinuities in the $P_n(m)$ distributions as a function of m. The magic compositions whose $P_n(m)$ values are irregularly larger than those of the smaller neighbors $P_n(m-1)$ and larger neighbors $P_n(m+1)$ are referred to as type **D** and **U**, respectively. Clusters in type **D** include $Co_5O_5^-$, $Co_6O_5^-$, $Co_7O_6^-$, $Co_7O_9^-$, $Co_8O_6^-$, $Co_8O_8^-$, $Co_9O_7^-$, and $Co_{10}O_7^-$. In contrast, clusters in type **U** include $Co_3O_5^-$, $Co_3O_6^-$, $Co_4O_7^-$, $Co_5O_6^-$, $Co_5O_8^-$, $Co_6O_6^-$,

$Co_6O_8{}^-$, $Co_7O_7{}^-$, $Co_7O_{10}{}^-$, $Co_8O_{11}{}^-$, $Co_9O_8{}^-$, $Co_9O_{12}{}^-$, $Co_{10}O_8{}^-$, and $Co_{10}O_{13}{}^-$. Small

magic compositions such as $Co_3O_4{}^-$, $Co_4O_4{}^-$, and $Co_4O_6{}^-$ cannot be categorized

unambiguously into **D** or **U**. The magic compositions observed in the present study are

plotted in Fig. 2.14. The downward and upward arrows in the figure indicate that the

compositions are in type **D** and **U**, respectively. The compositions of type **U** are divided

into oxygen-rich and oxygen-poor series except for $n = 4$ and 8: the one with $n{:}m$ ratio of

~3:4 (open diamonds in Fig. 2.14) and the other with ~1:1 (closed circles in Fig. 2.14).
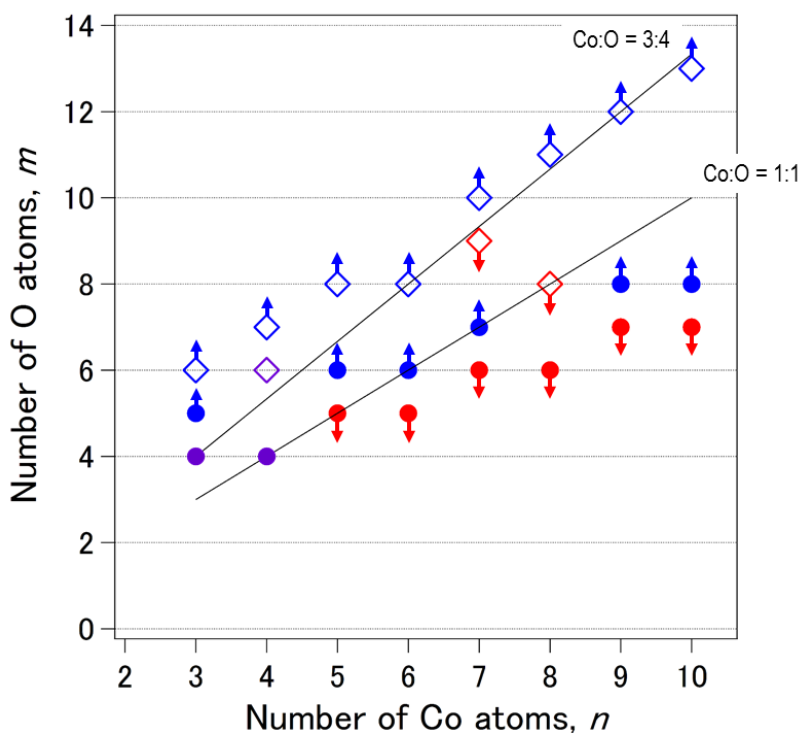

Figure 2.14. Plots of magic compositions for $Co_nO_m{}^-$. Circles and diamonds indicate the oxygen-poor and oxygen-rich magic compositions respectively. Downward and upward arrows correspond to the magic compositions of types **D** and **U**, respectively. See text for the definitions. The two lines represent compositions of $n{:}m = 1{:}1$ and 3:4.

2.3.2. Electronic structures of $Co_nO_m^-$

Fig. 2.15 shows the photoelectron spectra of $Co_nO_m^-$ ($n = 3$–9, $m = 0$–9) measured by using 4.66 eV photons. The photoelectron spectra of Co_n^- and $Co_nO_m^-$ ($m \leq 3$) quantitatively agreed with those in previous reports,[27,29–32,37,38] except for $Co_nO_3^-$ ($n = 4$, 5) and $Co_3O_1^-$. The AEAs of Co_nO_3 ($n = 4$, 5) were larger than those of the corresponding Co_nO_2, whereas the previous studies reported the opposite behavior due to the formation of the peroxo species $Co_nO(O_2)^-$. The different behavior suggests that $Co_nO_3^-$ ($n = 4$, 5) produced in our setup have different structures. Our PES data of $Co_3O_1^-$ was contaminated by signals from the Co_3OH^- impurity present in the beam as suggested by the peak at ~1.9 eV.[39] However, this contamination did not affect the determination of AEA of Co_3O_1 because Co_3OH has significantly higher AEA (~1.56 eV).[39] Overall, the spectra become featureless with an increase in the m value while the small oxygen-free Co_n^- exhibit characteristic peaks. This behavior might be due to an increase in the density of electronic states by hybridization of $Co(3d)$ and $O(2p)$ orbitals.

AEAs of Co_nO_m ($n = 3$–9, $m = 0$–9) were determined from the onsets of the PES bands by the method described in section 2.2.1. The AEA values thus estimated are listed in Table 2.1 and plotted in Fig. 2.16. Overall, the AEAs of Co_nO_m increased as the m values increased except on going from Co_8O_4 to Co_8O_5. The gradual increase of the AEAs with m implies sequential electron transfer from the Co cluster to the added O atoms. Fig. 2.16 (b) plots the difference of AEAs, $\Delta AEA(n, m)$ defined in eq. (2.11), as a function of m,

$$\Delta AEA(n, m) = AEA(n, m) - AEA(n, m - 1) \qquad (2.11)$$
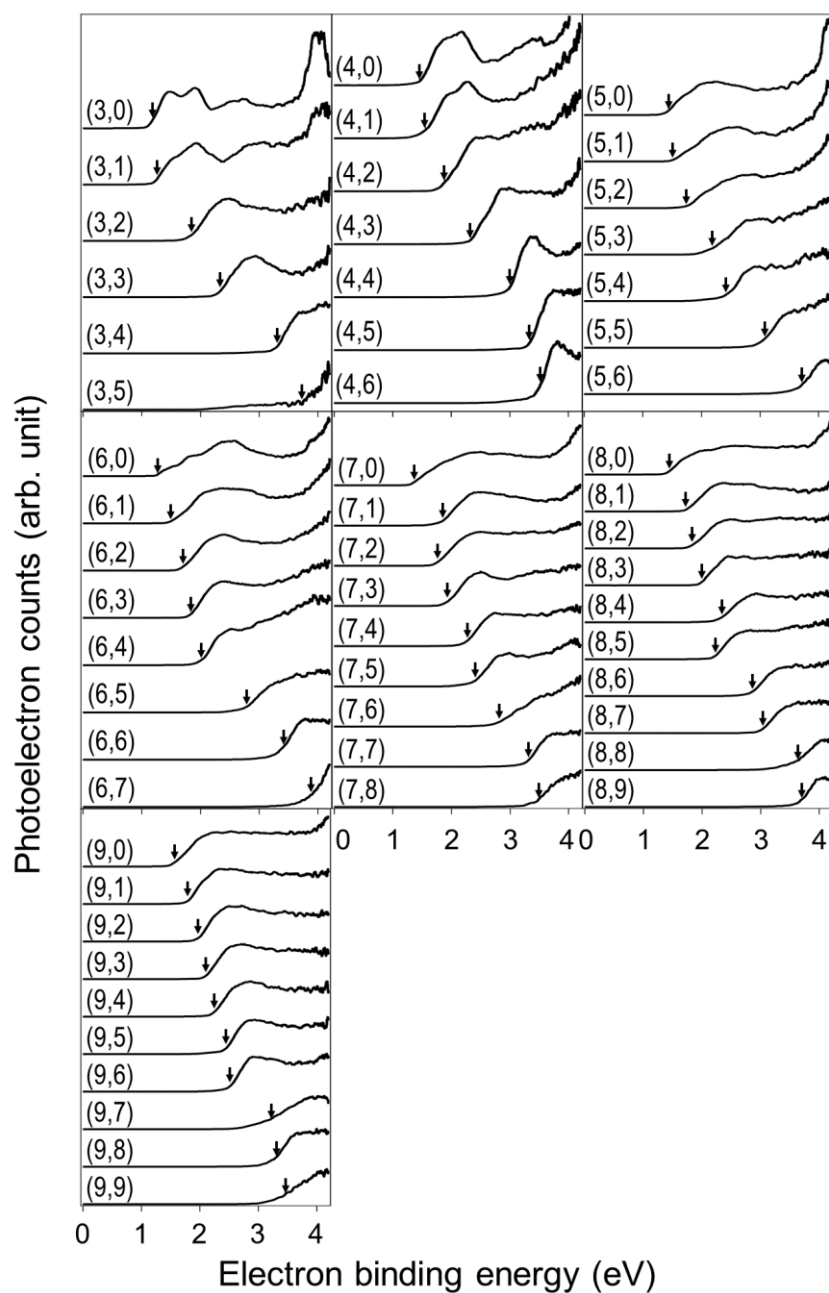
Figure 2.15. Photoelectron spectra of $Co_nO_m^-$ (n = 3–9, m = 0–9). The notation (n, m) represents the chemical compositions of $Co_nO_m^-$. Arrows indicate the AEAs.

The AEAs increased abruptly at the compositions of Co_3O_4, Co_4O_4, Co_5O_5, Co_6O_5, Co_8O_6, Co_8O_8, and Co_9O_7, which agree with those of type **D** except for Co_7O_6.

Table 2.1. Experimental AEA Value of Co_nO_m (n = 3–9, m = 0–9).[a]

$m \backslash n$	3	4	5	6	7	8	9
0	1.18	1.46	1.43	1.25	1.31	1.44	1.57
1	1.26	1.56	1.51	1.46	1.82	1.72	1.79
2	1.85	1.88	1.74	1.76	1.82	1.83	1.97
3	2.34	2.33	2.18	1.84	1.98	1.99	2.10
4	3.31	3.00	2.42	1.98	2.16	2.34	2.24
5	3.72	3.34	3.08	2.83	2.42	2.22	2.44
6		3.53	3.71	3.41	2.82	2.86	2.52
7				3.89	3.28	3.04	2.70
8						3.63	3.31
9						3.71	3.46

[a]Unit in eV.
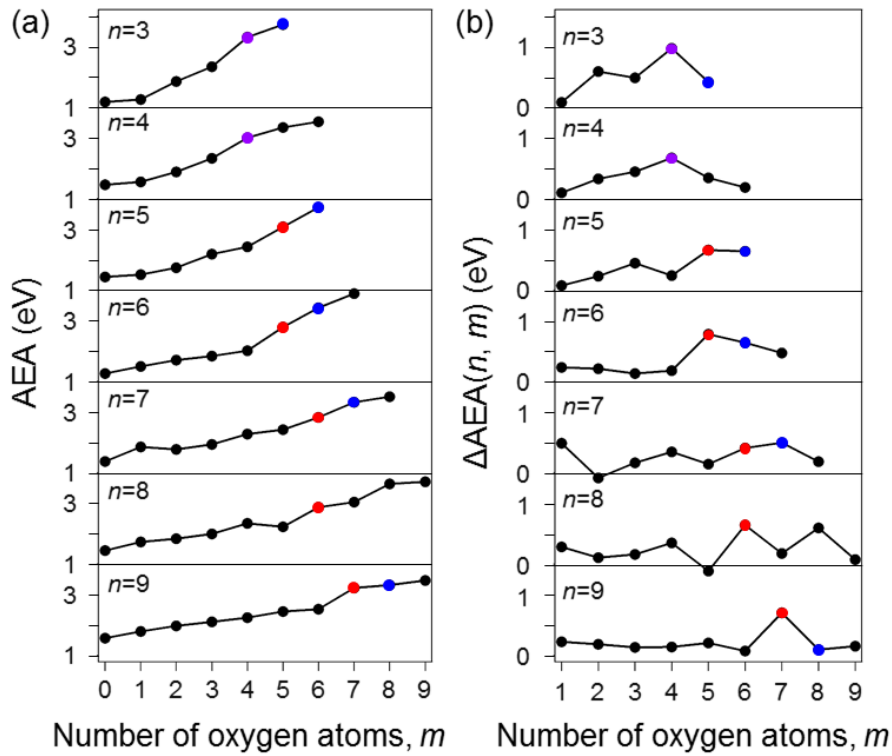
Figure 2.16. Plots of (a) AEA and (b) $\varDelta$AEA of Co_nO_m (n = 3–9, m = 0–9) as a function of m. Red and blue dots indicate the magic compositions of type **D** and **U**, respectively, whereas purple dots represent those whose type cannot be assigned unambiguously. See text for the definitions of type **U** and **D**.

2.3.3. Geometrical structures of $Co_nO_m^-$

In order to gain insight into the structural change at the initial stage of oxidation, the geometric and electronic structures were studied by DFT calculations taking $Co_7O_m^-$ (m = 0, 3–6) as an example. First, the structure of Co_7^- was re-optimized starting from the structures previously reported by changing the spin multiplicities (Fig. 2.17).[27] Two structural isomers, one with a capped octahedral structure Co_7^- **(1)** and the other with a pentagonal bipyramidal structure Co_7^- **(2)**, were obtained. It turned out that isomer Co_7^- **(1)** with the spin multiplicity of 15 was the most stable structure (Table 2.2). Thus, the structures of $Co_7O_m^-$ (m = 3–6) were optimized from initial structures in which O atoms were attached to Co_7^- **(1)** in a similar manner to cationic cobalt oxides previously reported.[14]
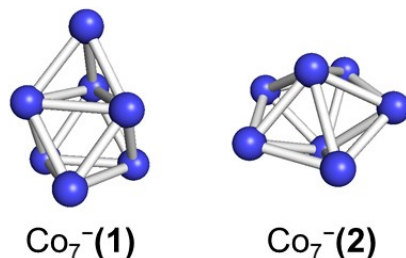
Figure 2.17. Optimized structures of Co_7^-.

Table 2.2. Relative Energies and Properties of Co_7^- Obtained from DFT Calculations.

	Co_7^- **(1)**	Co_7^- **(2)**
ΔE (eV) [a]	0	0.02
2S+1 [b]	15	15
AEA (eV) [c]	1.69	1.51
VDE (eV)	1.74	1.89
Co–Co$_{Ave}$ (Å) [d]	2.49	2.49

[a]Relative energy. [b]Spin multiplicity. [c]Adiabatic electron affinity of corresponding neutral [d]Average of bond length of Co–Co bonds.

Fig. 2.18 shows the optimized structures of the isomers of $Co_7O_m^-$ ($m = 3$–6) and isomer series **(1)** indicates most stable isomer. For $m = 3$, three O atoms selectively occupy nonadjacent facets of the octahedral Co_6 moiety. Two structural isomers were found for $m = 4$–6 (Tables 2.3 and 2.4). In all the structures, the O atoms were bound to the facets or edges of the tetrahedral Co_4 moiety via μ_3 and μ_2 modes, respectively, while retaining the structural motif of the $Co_7O_3^-$ moiety. The Co–O bonds of the μ_3 and μ_2 modes for $m = 4$–6 were in the ranges of 1.85–2.00 and 1.75–1.80 Å, respectively. The structure of $Co_7O_6^-$**(1)** shown in Fig. 2.18 suggests that preferential binding sites of the O atoms depend on the local structure of Co_7^-**(1)**: the facets for the octahedral Co_6 moiety and the edges for the tetrahedral Co_4 moiety. A previous theoretical study reports that O atoms prefer binding to the facets regardless of m in case of oxygen-poor $Co_7O_m^+$ cations ($1 \leq m \leq 5$).[14] The Co–Co bond lengths were elongated with an increasing the m values: the average length of the Co–Co bonds increased from 2.49 Å for Co_7^-**(1)** to 2.53, 2.71, 2.80, and 2.84 Å for in $Co_7O_3^-$**(1)**, $Co_7O_4^-$**(1)**, $Co_7O_5^-$**(1)**, and $Co_7O_6^-$**(1)**, respectively. Closer inspection revealed that the Co–Co bonds directly bonded to the O atoms were elongated. The VDEs, and total NBO charges of the Co_7 moiety of the most stable isomers of $Co_7O_m^-$ ($m = 3$–6) and AEAs of the corresponding neutrals are listed in Table 2.3. The AEA values of Co_7O_m increased with increase in m, which reproduces the general trend experimentally observed (Fig. 2.16 (a)). The trend in AEAs is consistent with sequential electron withdrawal from Co_7 by the O atoms, as shown in the NBO values.
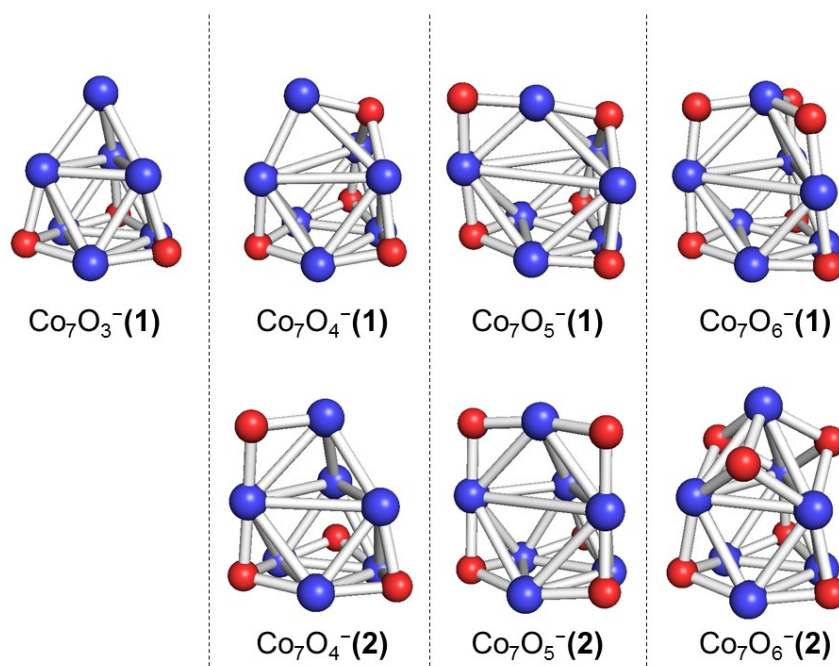
Figure 2.18. Optimized structures of $Co_7O_m^-$ (m = 3–6) obtained by DFT calculation.

Table 2.3. Relative Energy and Properties of $Co_7O_m^-$ (m = 3–6) Obtained from DFT Calculations.

|	$Co_7O_3^-$ **(1)**	$Co_7O_4^-$ **(1)**	$Co_7O_5^-$ **(1)**	$Co_7O_6^-$ **(1)**
ΔE (eV) [a]	0	0	0	0
2S+1 [b]	15	17	17	11
AEA (eV) [c]	1.78	2.18	2.53	2.82
VDE (eV)	2.00	2.34	2.82	3.29
NBO_{Co} [d]	2.50	3.79	4.83	5.52
Co–Co$_{Ave}$ (Å) [e]	2.53	2.71	2.80	2.84
		$Co_7O_4^-$ **(2)**	$Co_7O_5^-$ **(2)**	$Co_7O_6^-$ **(2)**
ΔE (eV) [a]		+0.38	+0.48	+0.71
2S+1 [b]		17	13	13
AEA (eV) [c]		2.11	2.69	3.91
VDE (eV)		2.21	2.92	5.21
NBO_{Co} [d]		3.56	4.58	6.01
Co–Co$_{Ave}$ (Å) [e]		2.61	2.68	2.69

[a]Relative energy among each isomer. [b]Spin multiplicity. [c]Adiabatic electron affinity of corresponding neutral. [d]Total NBO charge of Co core. [e]Average length of Co–Co bond.

Table 2.4. Relative Energies of $Co_7O_m^-$ (m = 0, 3–6) with Different Spin Multiplicities.[a]

	Spin multiplicity					
	9	11	13	15	17	19
Co_7^-**(1)**			0.714	0	0.401	
Co_7^-**(2)**			0.749	0	0.624	1.124
$Co_7O_3^-$**(1)**		0.106	0.681	0	0.420	
$Co_7O_4^-$**(1)**		0.512	0.449	0.795	0	
$Co_7O_4^-$**(2)**	0.582	1.557	1.262	0.207	0	0.699
$Co_7O_5^-$**(1)**		0.587	0.012	0.864	0	1.058
$Co_7O_5^-$**(2)**		0.220	0	1.129	b	
$Co_7O_6^-$**(1)**	0.662	0	0.055	1.386	0.647	
$Co_7O_6^-$**(2)**	2.671	0.676	0	1.295	0.696	

[a]Unit in eV. [b]Structure was transformed to $Co_7O_5^-$**(1)** during the optimization.

In order to see whether the above mechanism of the initial stage of the oxidation is applicable to other sizes, the structures of Co_6^- and $Co_6O_5^-$ were also examined by DFT calculations. Fig. 2.19 shows the optimized structures of Co_6^- and $Co_6O_5^-$ (Table 2.5). In $Co_6O_5^-$, four O atoms and one O atom are bound to the facets and edges of the octahedral Co_6 core. As can be seen, octahedral motif of Co_6 core is retained although the average Co–Co bond lengths were elongated from 2.47 Å for Co_6^- to 2.62 Å for $Co_6O_5^-$.
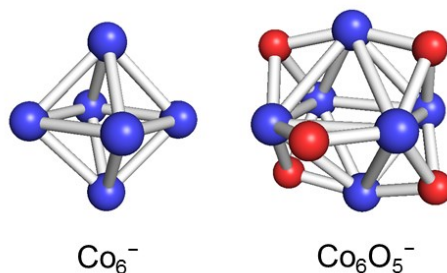
Co_6^- $Co_6O_5^-$

Figure 2.19. Optimized structures of Co_6^- and $Co_6O_5^-$ obtained by DFT calculation.

Table 2.5. Relative Energies of Co_6 and $Co_6O_5^-$ with Different Spin Multiplicities.[a]

	Spin multiplicity		
	12	14	16
Co_6^-	0.75	0	1.03
$Co_6O_5^-$	1.13	0.96	0

[a]Unit in eV.

2.4. Discussion

Magic compositions of $Co_nO_m^-$ produced in the early stage of the oxidation of Co_n^- were identified for the first time by investigating the population distributions of $Co_nO_m^-$ as a function of m (Fig. 2.14). In the following we discuss the origin of the two types of magic compositions **U** and **D**.

2.4.1. Magic compositions of full- and surface- oxidized species

Oxidation reactions of Co_n^- nascently produced cobalt oxide cluster anions $[Co_xO_y]^{-*}$ with large internal energy. Under our experimental conditions, collisional cooling could not completely suppress the fragmentation or etching of $[Co_xO_y]^{-*}$ by releasing Co containing species (Fig. 2.13).[18] It is plausible that O atoms were also dissociated in the relaxation processes of $[Co_xO_y]^{-*}$. Magic compositions of type **U** are associated with sudden decrease in the reaction rate for subsequent addition of O atom or in the binding energy of O atom.

We propose that two series of magic compositions with $n:m$ ratios of ~3:4 and ~1:1 have different origins. The oxygen-rich clusters such as $Co_3O_6^-$, $Co_4O_7^-$, $Co_5O_8^-$, $Co_6O_8^-$, $Co_7O_{10}^-$, $Co_8O_{11}^-$, $Co_9O_{12}^-$, and $Co_{10}O_{13}^-$ (open diamonds in Fig. 2.14) may correspond to fully oxidized states because the compositions are comparable to those of Co_3O_4 in the

bulk. Thus the appearance of these magic clusters is ascribed to the significant reduction of binding energies of O atoms to fully oxidized clusters. In contrast, oxygen-poor clusters such as $Co_3O_5^-$, $Co_5O_6^-$, $Co_6O_6^-$, $Co_7O_7^-$, $Co_9O_8^-$, and $Co_{10}O_8^-$ (closed circles in Fig. 2.14) may correspond to the intermediates of the full oxidation states. Given that oxidation proceeds by bonding O atoms on the facets or edges of Co_n^- while retaining its morphology (Fig. 2.18 and 2.19), one of the plausible models is that all surface sites of the clusters available for adsorption are occupied by O atoms. Their appearance is ascribed to the kinetic bottleneck against internal oxidation owing to significant structural change of the Co_n moiety.

2.4.2. Magic compositions of inert anions against electron emission

In contrast, magic compositions of type **D** are associated to the abrupt increase of survival probability as anionic states during the relaxation of $[Co_xO_y]^{-*}$. In fact, we observed that the AEA of Co_nO_m increased abruptly at the compositions of type **D** except Co_7O_6 (Fig. 2.16 (b)). This coincidence suggests that magic compositions of type **D** are electronically more stable than the smaller neighbors. High abundance of magic compositions $Co_nO_m^-$ is ascribed to that thermionic emission is slower than from $Co_nO_{m-1}^-$ due to higher electron affinity. It is concluded that the suppression of the electron detachment from $[Co_xO_y]^{-*}$ contributes to the appearance of magic compositions of $Co_3O_4^-$, $Co_4O_4^-$, $Co_5O_5^-$, $Co_6O_5^-$, $Co_8O_6^-$, $Co_8O_8^-$, and $Co_9O_7^-$. High abundance of the rest of compositions in type **D**, $Co_7O_6^-$, is ascribed to the retardation of fragmentation of O atoms.

2.5. Conclusions

We discovered magic compositions of $Co_nO_m{}^-$ produced by the exothermic reaction of $Co_n{}^-$ with O_2 using mass spectrometry and discussed the origin of their magic behavior using photoelectron spectroscopy and DFT calculation. Population analysis showed the two types of magic compositions (type **D** and **U**). Photoelectron spectroscopy indicated the abrupt increase of the AEA at compositions **D**, implying that clusters of composition **D** are relatively stable against thermionic emission reaction. The results of DFT calculations of $Co_7O_m{}^-$ and $Co_6O_m{}^-$ showed that the O atoms were sequentially attached to the surface of Co_7 and Co_6 cores, respectively. We propose that oxygen-poor and oxygen-rich compositions of type **U** correspond to surface oxidized and fully oxidized species, respectively.

References

1. Kalska, B.; Fumagalli, P.; Hilgendorff, M.; Giersig, M. *Mater. Chem. Phys.* **2008**, *112*, 1129.

2. Zhang, L.; Hu, P.; Zhao, X.; Tian, R.; Zou, R.; Xia, D. *J. Mater. Chem.* **2011**, *21*, 18279.

3. Liao, L.; Zhang, Q.; Su, Z.; Zhao, Z.; Wang, Y.; Li, Y.; Lu, X.; Wei, D.; Feng, G.; Yu, Q.; Cai, X.; Zhao, J.; Ren, Z.; Fang, H.; Robles-Hernandez, F.; Baldelli, S.; Bao, J. *Nat. Nanotechnol.* **2014**, *9*, 69.

4. Guo, S.; Zhang, S.; Wu, L.; Sun, S. *Angew. Chem., Int. Ed.* **2012**, *51*, 11770.

5. Bartling, S.; Yin, C.; Barke, I.; Oldenburg, K.; Hartmann, H.; Oeynhausen, V. Von; Pohl, M.; Houben, K.; Tyo, E. C.; Seifert, S.; Lievens, P.; Meiwes-Broer, K.-H.; Vajda, S. *ACS Nano* **2015**, 6, 5984.

6. Oliveira, M. C.; Marçalo, J.; Vieira, M. C.; Ferreiraac, M. A. A. *Int. J. Mass Spectrom.* **1999**, *185*, 825.

7. Yi, M. N.; Fisher, K. J.; Dance, I. G. *Int. J. Mass Spectrom.* **2002**, *216*, 155.

8. Johnson, G. E.; Reveles, J. U.; Reilly, N. M.; Tyo, E. C.; Khanna, S. N.; Castleman, A. W. *J. Phys. Chem. A* **2008**, *112*, 11330.

9. Yin, S.; Xue, W.; Ding, X.-L.; Wang, W.-G.; He, S.-G.; Ge, M.-F. *Int. J. Mass Spectrom.* **2009**, *281*, 72.

10. Xie, Y.; Dong, F.; Heinbuch, S.; Rocca, J. J.; Bernstein, E. R. *Phys. Chem. Chem. Phys.* **2010**, *12*, 947.

11. Dibble, C. J.; Akin, S. T.; Ard, S.; Fowler, C. P.; Duncan, M. A. *J. Phys. Chem. A* **2012**, *116*, 5398.

12. Ota, K.; Koyasu, K.; Ohshimo, K.; Misaizu, F. *Chem. Phys. Lett.* **2013**, *588*, 63.

13. Dijk, C. N.; Roy, D. R.; Fielicke, A.; Rasing, T.; Reber, A. C.; Khanna, S. N.; Kirilyuk, A. *Eur. Phys. J. D* **2014**, *68*, 357.

14. Aguilera-Del-Toro, R. H.; Aguilera-Granja, F.; Vega, A.; Balbás, L. C. *Phys. Chem. Chem. Phys.* **2014**, *16*, 21732.

15. Datta, S.; Rahaman, B. *AIP Adv.* **2015**, *5*, 117231.

16. Sun, Q.; Sakurai, M.; Wang, Q.; Yu, J. *Phys. Rev. B* **2000**, *62*, 8500.

17. Sakurai, M.; Sun, Q.; Sumiyama, K.; Kawazoe, Y. *Proc. Int. Symp. Clust. Assem. Mater.* **2001**, *3*, 158.

18. Kapiloff, E.; Ervin, K. M. *J. Phys. Chem. A* **1997**, *101*, 8460.

19. Murray, K. K.; Boyd, R. K.; Eberlin, M. N.; Langley, G. J.; Li, L.; Naito, Y. *Pure Appl. Chem.* **2013**, *85*, 1515.

20. Wiley, W. C.; McLaren, I. H. *Rev. Sci. Instrum.* **1955**, *26*, 1150.

21. Vorm, O.; Mann, M. *J. Am. Soc. Mass Spectrom.* **1994**, *5*, 955.

22. Zubarev, R. A.; Hakansson, P.; Sundqvist, B. *Rapid Commun. Mass Spectrom.* **1996**, *10*, 1386.

23. Green, F. M.; Gilmore, I. S.; Seah, M. P. *J. Am. Soc. Mass Spectrom.* **2006**, *17*, 514.

24. Shreve, A. T.; Yen, T. A.; Neumark, D. M. *Chem. Phys. Lett.* **2010**, *493*, 216.

25. Watanabe, T.; Tsukuda, T. *J. Phys. Chem. C* **2013**, *117*, 6664.

26. Muramatsu, S.; Koyasu, K.; Tsukuda, T. *J. Phys. Chem. A* **2016**, *120*, 957.

27. Yanagimachi, A.; Koyasu, K.; Valdivielso, D. Y.; Gewinner, S.; Schöllkopf, W.; Fielicke, A.; Tsukuda, T. *J. Phys. Chem. C* **2016**, *120*, 14209.

28. Arnold, D. W.; Bradforth, S. E.; Kim, E. H.; Neumark, D. M. *J. Chem. Phys.* **1995**, *102*, 3495.

29. Liu, S.-R.; Zhai, H.-J.; Wang, L.-S. *Phys. Rev. B* **2001**, *64*, 153402.

30. Yoshida, H.; Terasaki, A.; Kobayashi, K.; Tsukada, M.; Kondow, T. *J. Chem. Phys.* **1995**, *102*, 5960.

31. Yoshida, H.; Terasaki, A.; Kondow, T. *Surf. Rev. Lett.* **1996**, *3*, 667.

32. Pramann, A.; Koyasu, K.; Nakajima, A.; Kaya, K. *J. Phys. Chem. A* **2002**, *106*, 4891.

33. Gutsev, G. L.; Jena, P.; Zhai, H.-J.; Wang, L.-S. *J. Chem. Phys.* **2001**, *115*, 7935.

34. Frisch, M. J.; Trucks, G. W.; Schlegel, H. B.; Scuseria, G. E.; Robb, M. A.; Cheeseman, J. R.; Scalmani, G.; Barone, V.; Mennucci, B.; Petersson, G. A.; Nakatsuji, H.; Caricato, M.; Li, X.; Hratchian, H. P.; Izmaylov, A. F.; Bloino, J.; Zheng, G.; Sonnenberg, J. L.; Hada, M.; Ehara, M.; Toyota, K.; Fukuda, R.; Hasegawa, J.; Ishida, M.; Nakajima, T.; Honda, Y.; Kitao, O.; Nakai, H.; Vreven, T.; Montgomery, J. A., Jr.; Peralta, J. E.; Ogliaro, F.; Bearpark, M.; Heyd, J. J.; Brothers, E.; Kudin, K. N.; Staroverov, V. N.; Kobayashi, R.; Normand, J.; Raghavachari, K.; Rendell, A.; Burant, J. C.; Iyengar, S. S.; Tomasi, J.; Cossi, M.; Rega, N.; Millam, J. M.; Klene, M.; Knox, J. E.; Cross, J. B.; Bakken, V.; Adamo, C.; Jaramillo, J.; Gomperts, R.; Stratmann, R. E.; Yazyev, O.; Austin, A. J.; Cammi, R.; Pomelli, C.; Ochterski, J. W.; Martin, R. L.; Morokuma, K.; Zakrzewski, V. G.; Voth, G. A.; Salvador, P.; Dannenberg, J. J.; Dapprich, S.; Daniels, A. D.; Farkas, Ö.; Foresman, J. B.; Ortiz, J. V.; Cioslowski, J.; Fox, D. J. *Gaussian 09*, Revision C.01, Gaussian, Inc., Wallingford CT, 2011.

35. Glendening, E. D.; Reed, A. E.; Carpenter, J. E.; Weinhold, F. *NBO*, version 3.1.

36. *The PyMOL Molecular Graphics System*, version 1.8; Schrödinger, LLC.

37. Liu, S.-R.; Zhai, H.-J.; Wang, L.-S. *Phys. Rev. B* **2002**, *65*, 113401.

38. Li, R.-Z.; Liang, J.; Xu, X.-L.; Xu, H.-G.; Zheng, W.-J. *Chem. Phys. Lett.* **2013**, *575*, 12.

39. Li, R.-Z.; Xu, H.-G.; Xu, X.-L.; Zheng, W.-J. *Chem. Phys. Lett.* **2014**, *607*, 105.

Chapter 3.

Oxidation reaction of iridium clusters

3.1. Introduction

Understanding of the structures of metal oxide clusters provides molecular-level picture on catalytically active sites. Ion mobility spectrometry (IMS) and vibrational spectroscopy have revealed that preferential bonding motif of oxygen atoms on metal clusters as a function of the number of O atoms. For example, O atoms take μ_2 or μ_3 bonding motif (Scheme 1) on the surface of Co cluster anions at the early stage of the oxidation (chapter 2). In the oxidation of Rh oxide cluster cations, the O atoms take μ_2 or μ_3 bonding motif at early stage of oxidation,[1,2] whereas on-top bonding motif on a terminal site and molecular-like η^2-oxygen can be seen in the oxygen-rich region such as $Rh_6O_{10}^+$ and $Rh_6O_{12}^+$, respectively. Similar trend was observed for other metal oxide clusters M_nO_m: the μ_2 or μ_3 motif dominates the structure of M_nO_m (M = Fe, Co, Ni and Zn) with $n:m \sim 1:1$,[3–6] and on-top motif in addition to μ_2 or μ_3 motif were observed in M_nO_m (M = Ti, V, Cr and Nb) with $n:m \sim 1:2–2.5$,[7–12] and molecular-like η^2-oxygen was also contained in the more oxygen-rich compositions. On the other hand, theoretical calculation proposed that the on-top oxygen bonding motif on a terminal site is favored in case of oxygen-poor iridium oxide clusters while μ_2 motif is dominant in the oxygen-rich composition.[13,14] However, there are few experimental reports on the formation and structures of isolated iridium oxide clusters in gas phase. Iridium has a possibility to have novel oxygen bonding motif in the small size clusters and new reaction site for catalytic reactions.

While experimental investigations of size-selected Ir clusters are limited to few studies so far, the structural prediction of them has been conducted by theoretical calculations.[15–22] Theoretical calculations suggested that Ir clusters with 1–48 atoms have simple cubic based structures,[17] while bulk and nanoparticle of Ir metal have face-

Scheme 3.1. Bonding motif of oxygen atoms on metal cluster surface.
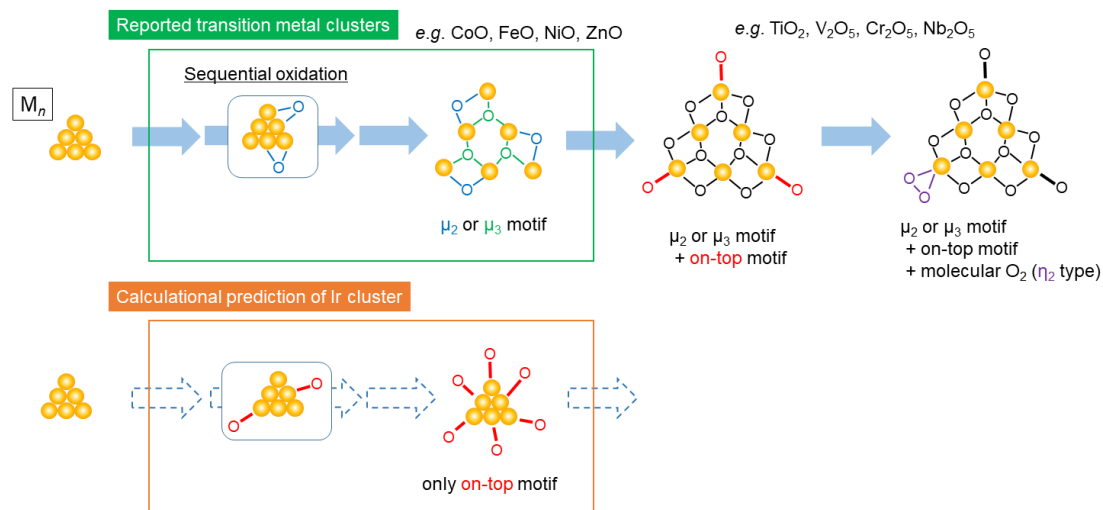
centered cubic structures.[23–26] Other metals in platinum group such as Ru, Rh, Os and Pt also showed the simple cubic structures at certain sizes.[15,18,19,27–30] The simple cube acted as a building unit of the cluster due to the stability of the square planer structure and this characteristic feature was explained by the localization of d orbitals and the electronic structure,[18] or the balance between the covalency and the Pauli repulsion.[19]

In addition to theoretical calculation, size-selected iridium clusters generated in gas-phase and liquid-phase have been applied for the variety of catalytic reactions such as ethylene hydrogenation and water oxidation and so on.[14,25,31,32] It was reported that the surface of Ir cluster encapsulated within dendrimer was partially oxidized according to XPS results and that the coexistence of the metal phase and oxidized phase contributed to the high selectivity on the hydrogenation reaction of nitroaromatics.[25] Therefore, fully- and partly-oxidized iridium clusters are both important for the development of the iridium cluster catalysts.

In this chapter, I investigated the structures of the iridium oxide cluster anions $Ir_nO_m{}^-$

(n = 4–8, m = 1–15) together with those of unoxidized iridium cluster anions Ir_n^- by conducting IMS and DFT calculation. It was found that Ir core favored cubic motif and that oxygen atoms favored bonding to the terminal site of the Ir core as the on-top motif. Interestingly, the collision cross section (CCS) of the octamers $Ir_8O_m^-$ decrease suddenly at m = 11. This structural transition is associated with the change in the binding motif of O atoms: from on-top bonding to the bridging μ_2 bonding.

3.2. Methods
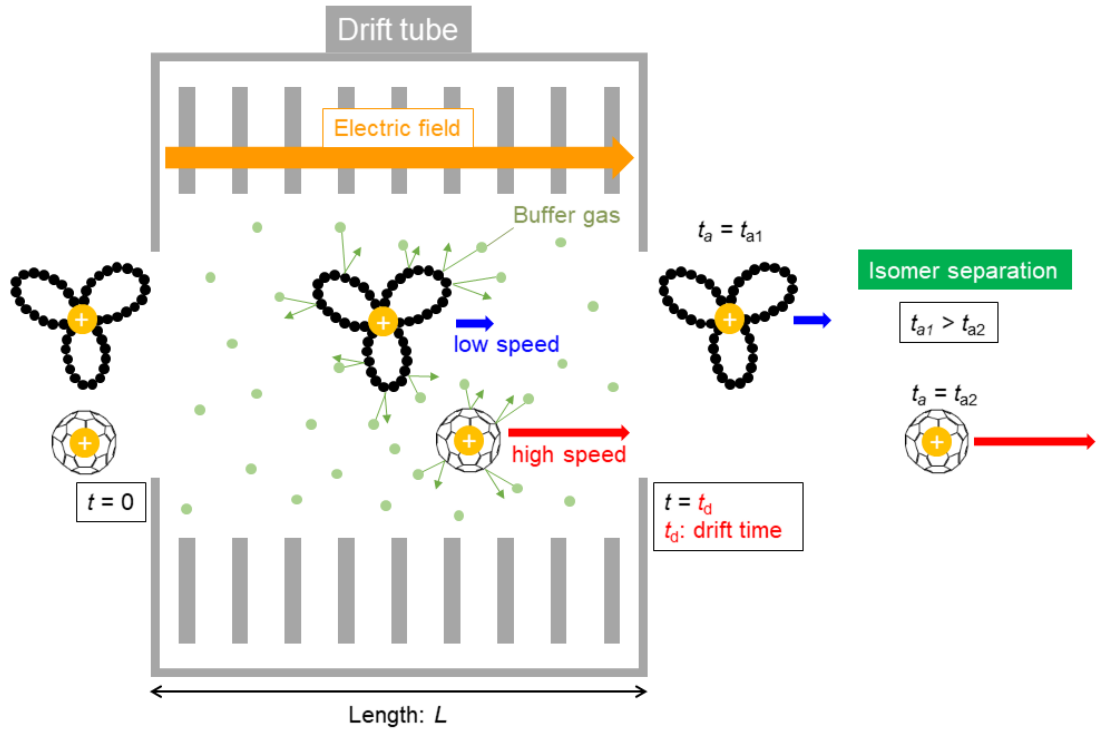
3.2.1. Ion mobility spectrometry (IMS)

3.2.1.1. Principles of operation

IMS is a powerful method to determine structural motif of the cluster ions.[33–35] The operation principles are explained in the following (Fig. 3.1). First, the cluster ions are injected into a drift cell filled with buffer gas. The ions travel in the cell with a "drift velocity (v_d)" determined by the balance between the acceleration by the electric field and deceleration by the collision with buffer gas. The drift velocity is given by,

$$v_d = KE \tag{3.1}$$

where K and E are ion mobility and the strength of electric field, respectively. Thus, structure isomers spend different drift time (t_d) depending on the morphologies as eq. (3.2),

$$t_d = \frac{L}{v_d} \tag{3.2}$$

Figure 3.1. Schematic image of ion mobility spectrometry.

where L is the length of the cell. Therefore, one can determine ion mobility K by measuring t_d. The CCS value (Ω) can be detremined by ion mobility K according to eq. (3.3),

$$\Omega \; = \; \frac{3e}{16N} \left(\frac{2\pi}{k_B \mu T_{eff}}\right)^{\frac{1}{2}} \frac{1}{K} \tag{3.3}$$

$$T_{eff} \; = \; T + \frac{M v_d{}^2}{3k_B} \tag{3.4}$$

where e, N, k_B, μ, T_{eff} are elementary charge, number of density, Boltzmann constant, reduced mass of the mass of target ion (m) and mass of buffer gas (M), and effective

temperature, respectively. Effective temperature (T_{eff}) is defined as eq. (3.4). Effective temperature is the summation of the temperature of buffer gas and effect of collision as written in eq. (3.4). Eq. (3.3) is valid only in low electric field condition such as $E/N <$ ~6–20 Td (1 Td = 10^{-17} Vcm^2):[10,33,36] the ion mobility is dependent on the electric field under the high electric field condition. The conditions employed in this work satisfy the above requirements because the E/N value was estimated to be 9.5 Td.

3.2.1.2. Experimental setup

Experimental apparatus installed at Tohoku University[3] is composed of three parts: a cluster source, an ion drift cell for IMS and a reflectron-type TOF-MS (Fig. 3.2). Iridium and iridium oxide cluster anions were generated by the laser vaporization method: The output of the second harmonic of a Nd:YAG laser (532 nm) was focused onto an Ir rod (99.9%; φ = 5 mm) under a pulsed O_2-seeded He carrier gas. Stagnation pressure of the carrier gas and the concentration of O_2 were tuned in the ranges of 0.3–0.6 MPa and 0–5%, respectively, in order to vary the composition of metal oxide clusters over a wide range. The generated iridium oxide cluster anions were injected with a kinetic energy of 50 eV into the ion drift cell filled with 2.00 Torr of helium buffer gas by a pulsed electric field. The electric field of 10 V/cm was applied to the 100 mm long ion drift cell, which was cooled to 170 K by using liquid nitrogen. Under this condition, E/N value was estimated to be ~9.5 Td, which could be thought as the low electric field condition as explained in previous section.[10,36] After exiting the ion drift cell, the ions were reaccelerated by another pulsed electric field and extracted into the TOF-MS. In this thesis, the time difference between the ion injection pulse into the drift cell and the reacceleration pulse was treated as the arrival time which was used in the calculation of
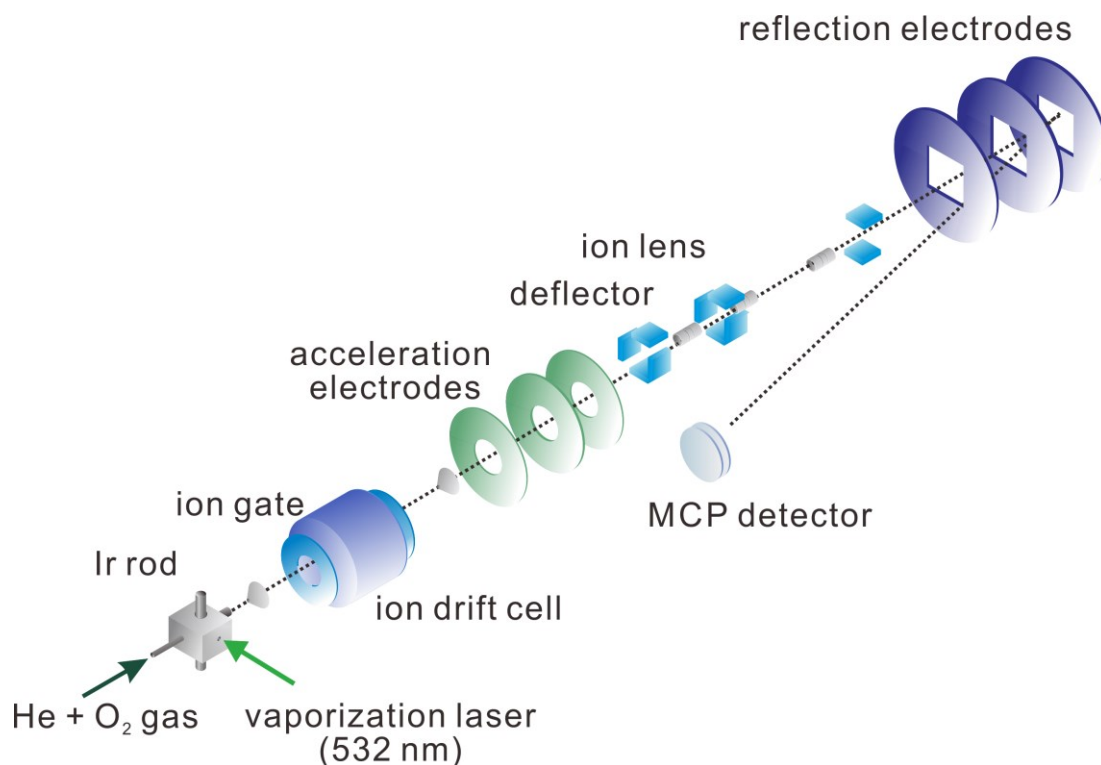
Figure 3.2. Schematic image of the experimental apparatus.

the experimental CCS value. A series of mass spectra was obtained by surveying the arrival time (t_a) systematically. An ion drift time (t_d), *i.e.* the time that the ions spent in the ion drift cell, was derived by subtracting the time that the ions took to flow outside of the cell from their arrival time[37] as written in eq. (3.5) and Fig. 3.3,

$$t_d = t_a - (t_{ig} + t_{skim} + t_{acc}) \qquad (3.5)$$

where t_{ig}, t_{skim} and t_{acc} represent the time consumed in ion gate, between end of ion drift cell and skimmer aperture, and between skimmer aperture and acceleration electrodes,
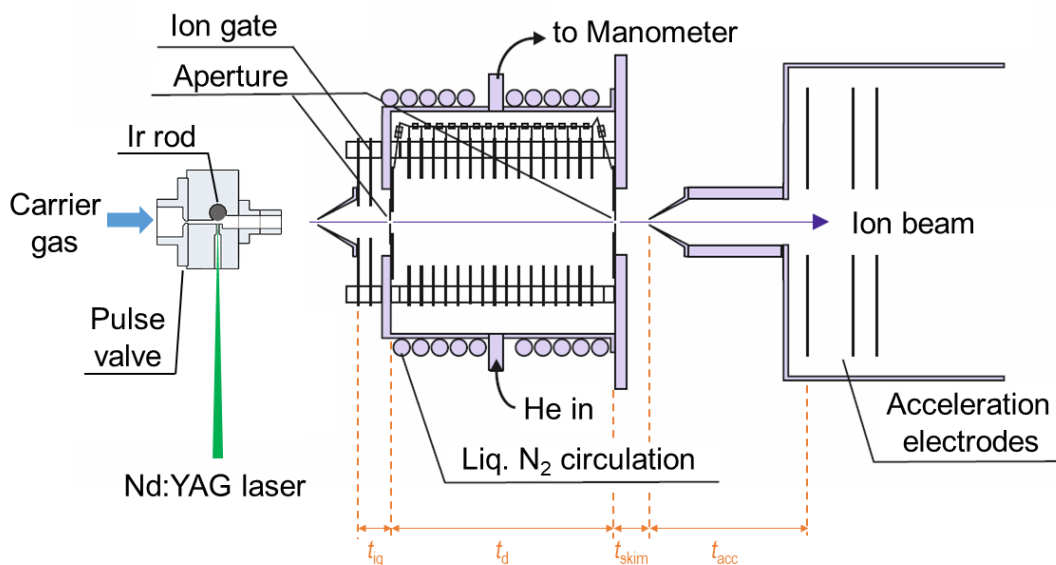
Figure 3.3. Schematic image of the ion drift cell.

respectively. The drift velocity was calculated by dividing the length of the ion drift cell by the ion drift time and converted to the ion mobility and CCS by using the eqs. (3.1), (3.2) and (3.3). A mass spectrum was also obtained by summing up all the mass spectra of each arrival time. Mass spectra in this thesis were calibrated by the spectra of cerium oxide cluster cations obtained under the same condition.

3.2.2. Theoretical calculations

The geometric and electronic structures of Ir_n^- and $Ir_nO_m^-$ were investigated by the DFT calculation with B3LYP as a functional and def-SV(P), which contains relativistic pseudopotentials of heavy element such as Ir, as a basis set.[38,39] The spin multiplicities were surveyed in the range of 1–17. Vibrational frequencies were also calculated to confirm that the optimized structures correspond to local minimum structures. In the calculation of the relative energies, the zero-point energy was considered. The charge on

each atom was estimated by using natural population analysis. In order to reduce computational costs for two-electron integrals and to accelerate structural and vibrational calculations, the resolution of identity approximation[40] was applied in all calculations. All calculations were carried out using the Turbomole 7.2.[41] The calculated structures were visualized using PyMOL.[42]

In order to identify the structures of Ir_n^- and $Ir_nO_m^-$ based on their experimental CCSs, the CCSs of the optimized structures were calculated. In this study, the CCSs were estimated by applying projection approximation (PA) method[43] using MOBCAL software developed by Jarrold.[44,45] In the PA method, the area of the projection image of the target cluster at a certain orientation is calculated with Monte Carlo method. Note that the each radius of the sphere using in projection is the sum of the radius of target element (Ir) and the radius of buffer gas element (He). By changing structure orientation and repeating Monte Carlo method, theoretical value of collision cross section is calculated. Therefore, the structure of the cluster and van der Waals radii of the target atom are key parameter of the calculation by the PA method.

3.3. Results and Discussion

3.3.1. Geometric structures of Ir_n^-

Fig. 3.4 shows a typical mass spectrum of Ir_n^- (n = 2–20) measured by using pure He carrier gas. In the spectrum, some magic behaviors could be recognized at n = 3, 7, and 9. The reproducibility of the relative intensity in $n \geq 10$ was poor due to low intensity and S/N ratio. The Ir atoms in the clusters take $6s^1(5d, 6p)^8$-like electron configuration according to previous report,[20] although the electron configuration of an isolated Ir atom is $6s^2 5d^7$. As a result, even-numbered clusters were more stable than odd-numbered
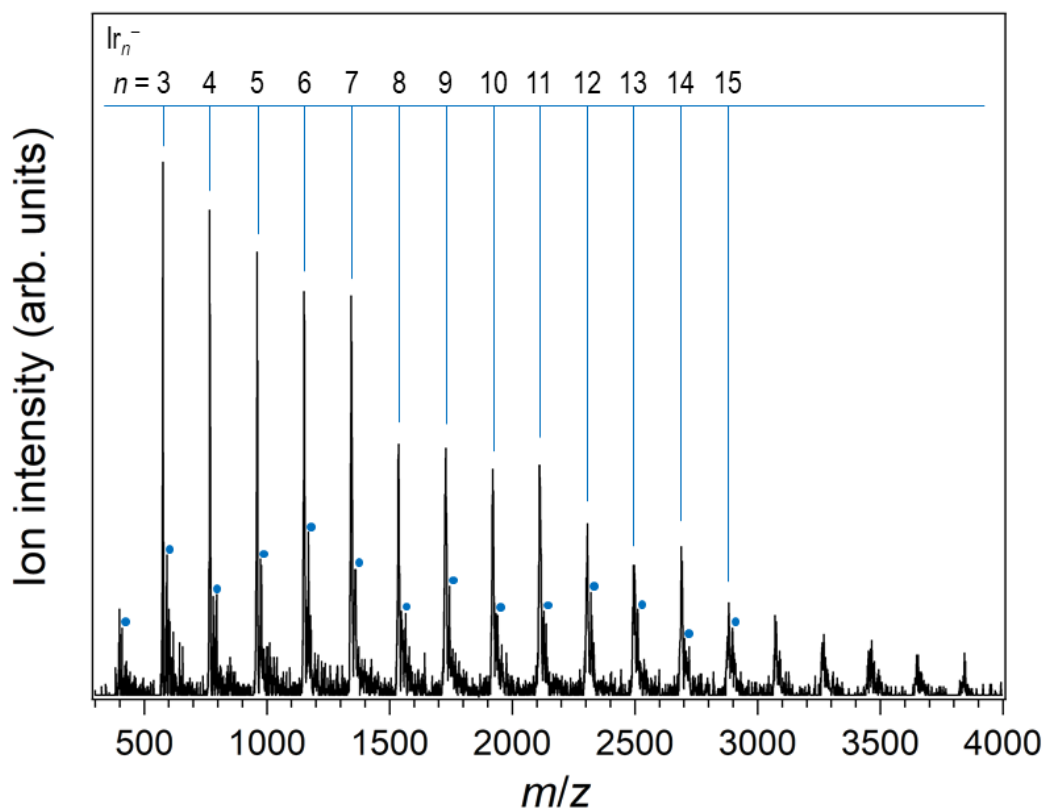
Figure 3.4. Mass spectra of Ir_n^- ($n = 2–20$). The peaks with the dot represent Ir_nO^-.

clusters in the case of neutral clusters due to the shell closure of delocalized s electrons. In a similar manner, the magic behavior of anionic Ir_n^- clusters at $n = 3, 7$ and 9 is attributed to the electronic shell closing. In the mass spectrum, small peaks assigned to the $Ir_nO_m^-$ ($m = 1, 2$) were also observed probably due to residual water on the inner wall of the stainless tube used for gas supply and oxide layer on the surface of Ir rod.

Arrival time distributions of Ir_n^- were shown in Fig. 3.5 as a function of n and the experimental CCSs were plotted in Fig. 3.6 as the black circles. The CCSs of Ir_n^- are monotonically increased with increase of n. I conducted the DFT calculation of Ir_n^- and obtained the structures as shown in Fig. 3.7. Relative energies of isomers with different spin multiplicities in each n are compared in Table 3.1. Basically, the structures of the
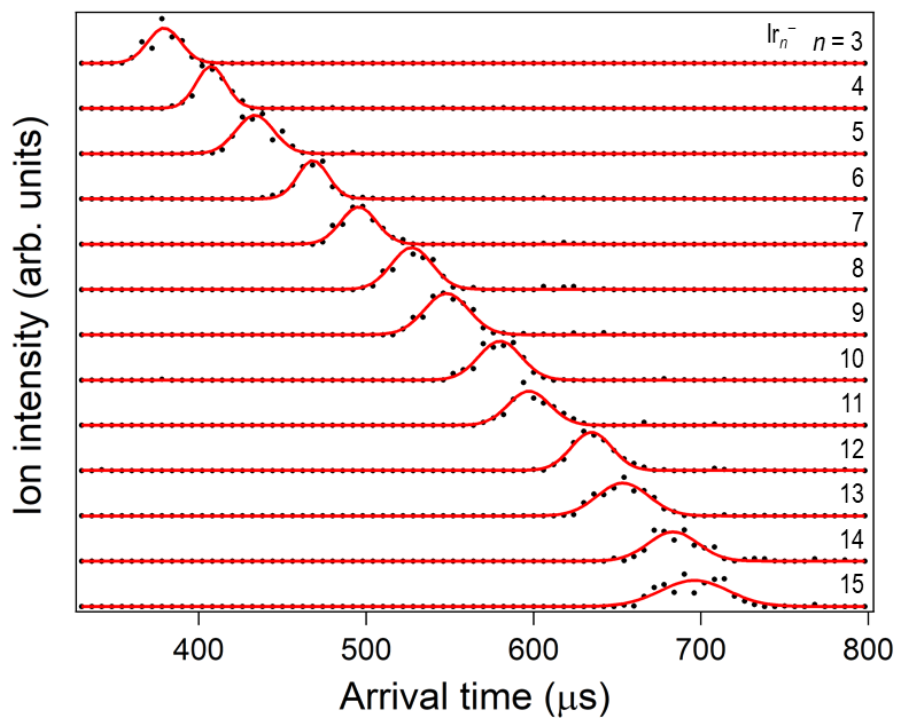
Figure 3.5. Arrival time distributions of Ir_n^- ($n = 3$–15).
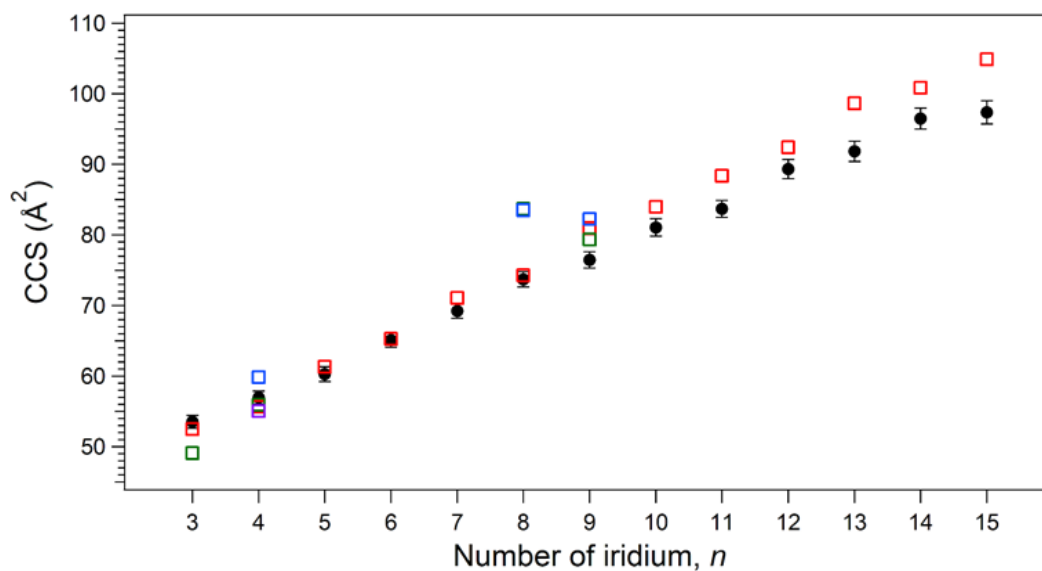
Figure 3.6. CCSs of Ir_n^- ($n = 3$–15). Black circles indicate the experimental value. Red, green, blue and purple squares indicate the calculated value isomers 1–4, respectively.
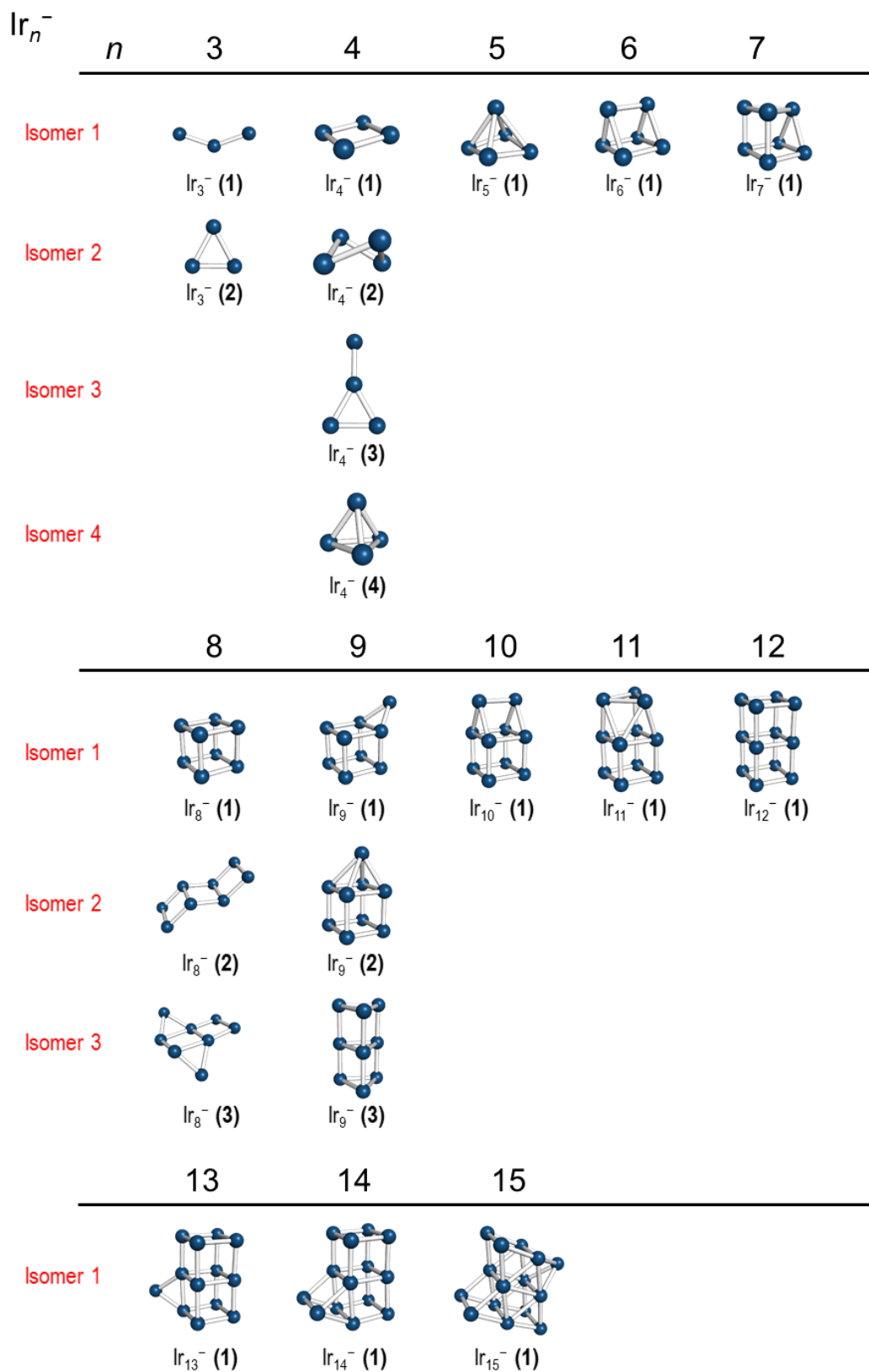
Figure 3.7. Optimized structures of Ir_n^- (n = 3–15).

Table 3.1. Relative Energies of Ir_n^- (n = 3–15) with Different Spin Multiplicities.[a]

	Spin multiplicity								
	1	3	5	7	9	11	13	15	17
Ir_3^- **(1)**	0.73	0.30	0.29	0	[b]				
Ir_3^- **(2)**	1.30	0.81	0.57	0.45	0.51				
Ir_5^- **(1)**	1.26	0.68	0.61	0.57	0.23	0.12	0	1.67	
Ir_7^- **(1)**	1.34	0.53	0.42	0.29	0.13	0.11	0.06	0	0.93
Ir_9^- **(1)**	0.47	0.05	0	0.01	0.04				
Ir_9^- **(2)**	1.35	0.30	0.39	0.32	0.41				
Ir_9^- **(3)**	1.41	0.66	0.59	0.58	0.61				
Ir_{11}^- **(1)**	0.74	0.07	0.13	0	0.22				
Ir_{13}^- **(1)**	0.55	0.03	0.05	0.00	0	0.11			
Ir_{15}^- **(1)**	1.12	0	0.13	0.09	0.12				

	Spin multiplicity					
	2	4	6	8	10	12
Ir_4^- **(1)**	0.97	0.41	0.26	0	0.02	[b]
Ir_4^- **(2)**	1.38	[b]	1.08	[b]	0.66	1.20
Ir_4^- **(3)**	1.18	1.19	0.89	0.94	1.10	
Ir_4^- **(4)**	1.71	1.68	[b]	[b]		
Ir_6^- **(1)**	0.40	0.32	0.19	0	0.07	
Ir_8^- **(1)**	0.06	0.16	0	0.10	0.01	
Ir_8^- **(2)**	2.10	2.02	1.89	1.89	1.87	2.11
Ir_8^- **(3)**	2.58	2.74	2.84	2.56	2.50	2.59
Ir_{10}^- **(1)**	0.19	0.01	0.06	0.01	0	0.01
Ir_{12}^- **(1)**	0.00	0.04	0	0.12	0.17	
Ir_{14}^- **(1)**	0.01	0.05	0	0.09	0.14	

[a]Unit in eV. [b]Structure was transformed to different motif during the optimization.

neutral Ir clusters reported previously[20] were used as initial structure for the optimization. The CCS values of several isomers were also calculated for $n = 3, 4, 8$ and 9. Among the isomers, the structures similar to those of neutral clusters were obtained as the most stable structure except for $n = 3$: Ir_3^- with a slightly bent structure was more stable than that with triangle or linear structure which is most stable in the neutral state. The calculated CCS values were listed in Table 3.2 and plotted in Fig. 3.6 as the colored squares. The radii of He and Ir were set to be 1.15 Å[10,43,46] and 1.93 Å, respectively, so that the calculated CCS agrees with the experimental CCS at $n = 6$. The CCS values of most stable structures were well matched with experimental values in $n \leq 8$ and a series of the optimized structures suggested the formation of the simple cubic Ir_8^- structure in sharp contrast to fcc structure of bulk and NPs of Ir. In the present study, the calculated CCS values were larger than the experimental values in $n \geq 9$. There are three possible reasons for this discrepancy. First, the difference may result from the overestimation of effective atomic radii for anionic clusters in large size region. Electron cloud in an anionic cluster is more extended than that in the corresponding neutral cluster due to "electron spill-out".[46,47] The effect of anionic surplus electron is weaker when there is a large total number of valence electrons and it might cause the overestimation of effective radii of Ir atom. Second, anionic clusters take more compact structures such as face-capped cubes like isomer 2 of Ir_9 in present experimental condition. Finally, spin-orbit (SO) coupling might affect the calculation of the optimized structure. In the present calculation, the one-component level calculation, which does not include SO effect, was conducted in order to reduce the calculation cost. As a general trend, Jahn-Teller distortion can be overestimated in the one-component level (without considering SO), while highly symmetric isomers can be favored under the two-component calculation (with

Table 3.2. Experimental and Calculated CCS Values of Ir_n^- ($n = 3$–15).[a]

| n	3	4	5	6	7
Exp.	53.5±0.9	57.0±0.9	60.3±1.1	65.1±1.1	69.2±1.0
Calc. (Isomer 1)	52.48	55.65	61.31	65.27	70.45
Calc. (Isomer 2)	49.07	55.91			
Calc. (Isomer 3)		59.82			
Calc. (Isomer 4)		55.03			
n	8	9	10	11	12
Exp.	73.7±1.1	76.5±1.1	81.1±1.2	83.7±1.2	89.3±1.4
Calc. (Isomer 1)	74.25	80.94	83.96	88.36	92.4
Calc. (Isomer 2)	83.70	79.35			
Calc. (Isomer 3)	83.50	82.26			
n	13	14	15		
Exp.	91.8±1.5	96.5±1.5	97.4±1.6		
Calc. (Isomer 1)	98.65	100.83	104.90		

[a]Unit in $Å^2$.

considering SO) due to the stabilization by SO splitting of the orbitals.[48,49]

3.3.2. Geometric structures of $Ir_nO_m^-$

Ir oxide clusters $Ir_nO_m^-$ were produced by seeding oxygen to the carrier He gas. The O$_2$ concentration was adjusted to obtain the experimental CCSs in a wide range of composition. Fig. 3.8 shows the typical mass spectra of $Ir_nO_m^-$ ($n = 3$–8, $m = 0$–15) obtained by using He carrier gas containing 0–5.0 % of O$_2$. Experimental CCSs of $Ir_nO_m^-$ are plotted as a function of m in Fig. 3.9. It is concluded within the accuracy of the
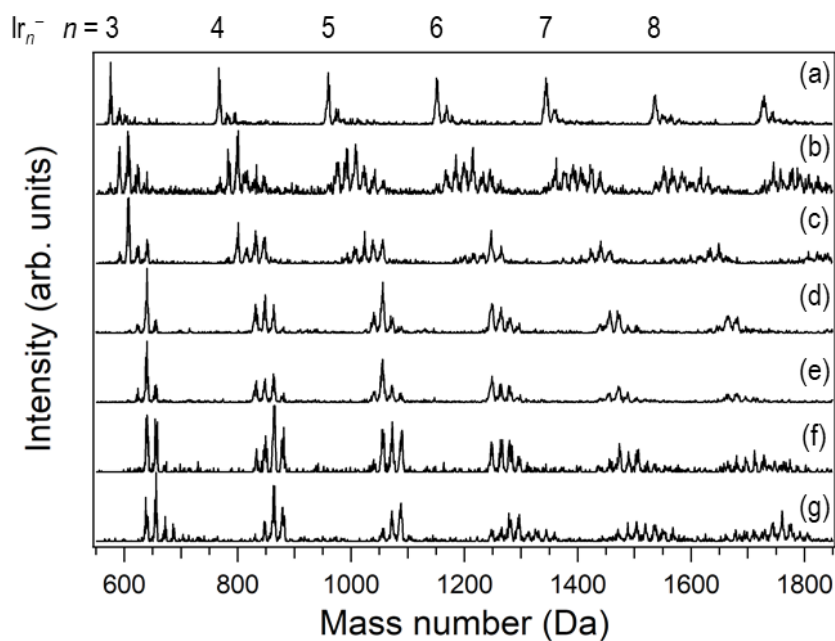
Figure 3.8. Mass spectra of $Ir_nO_m^-$ ($n = 3$–8, $m = 0$–15) obtained by using He carrier gas containing (a) 0, (b) 0.01, (c) 0.05, (d) 0.5, (e) 1.0, (f) 2.5, and (g) 5.0 % of O_2.
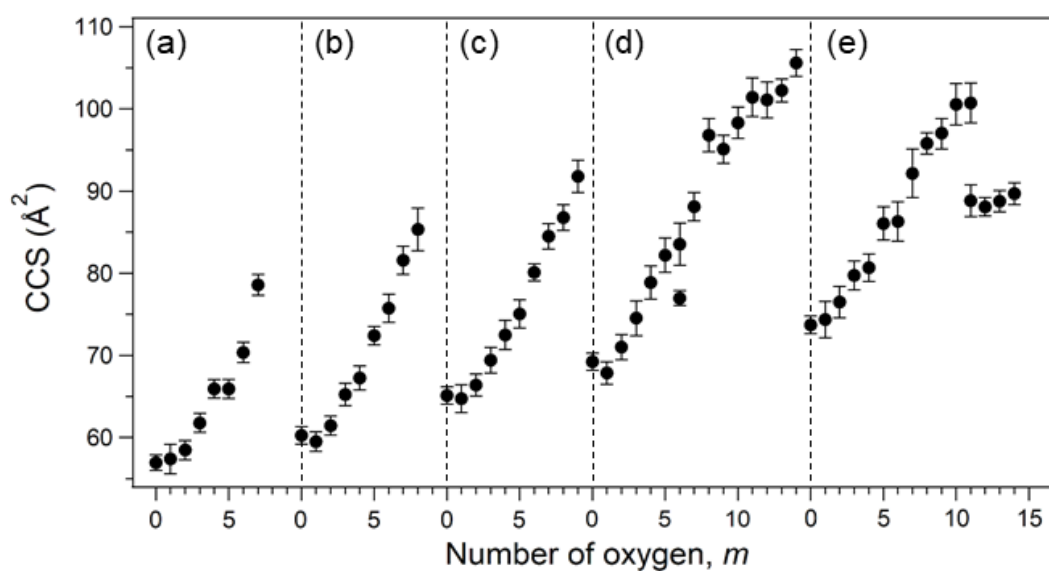
**Figure 3.9.** Experimental CCS values of $Ir_nO_m^-$ with (a) $n = 4$, (b) 5, (c) 6, (d) 7, and (e) 8 as a function of m.

measurements that the CCS values are monotonically increased with increase in m except for few cases. $Ir_7O_6^-$ and $Ir_8O_{11}^-$ had additional structural isomers having smaller CCS values. Drastic decrease of CCS at $Ir_8O_{11}^-$ indicated the large structural transition from bulky to compact structures occurred at this composition. In order to explain the evolution of the structural motif of $Ir_nO_m^-$, the experimental CCS values of $Ir_nO_m^-$ with $n = 5$ and 8 are compared with theoretical CCS values. Because of the limited computational resource, we chose $Ir_5O_m^-$ to gain insight into the gradual increase of the CCS values with increasing m. With the binding motif of O atoms in hand, we addressed the sudden decrease of the CCS values of $Ir_8O_m^-$ at $m = 11$.

3.3.2.1. $Ir_5O_m^-$

Optimized structures of several isomers (isomer 1 to 4) of $Ir_5O_m^-$ obtained by DFT calculation were shown in Fig. 3.10. Relative energies of isomers with different spin multiplicities in each n are compared in Table 3.3. The most stable isomers (isomer 1) were obtained by using the structures reported previously[13] as initial structures. Oxygen atoms were bonded to terminal site of the Ir_5 core as on-top motif in $m = 1$–5, whereas bridging (μ_2) motif was dominant in $n = 6$–8. The Ir_5 core motif of isomer 1 changes depending on m; square pyramid ($m = 0$–2), triangle bipiramid ($m = 3$–5) and sheet like structure ($m = 6$–8). The preferable spin states change depending on the degree of oxidation (m) as reported in Cr_nO_m.[50] In order to compare the CCS values of the structures with different oxygen bonding motif, I also calculated the CCS values for isomers 2–4. One or two bridging oxygen with triangle bipyramidal Ir_5 core, all on-top oxygen with tri-triangle Ir_5 core and all on-top oxygen with bi-triangle-one-top Ir_5 core were obtained as the isomer 2, 3 and 4, respectively. To reduce the computational cost, spin-multiplicity
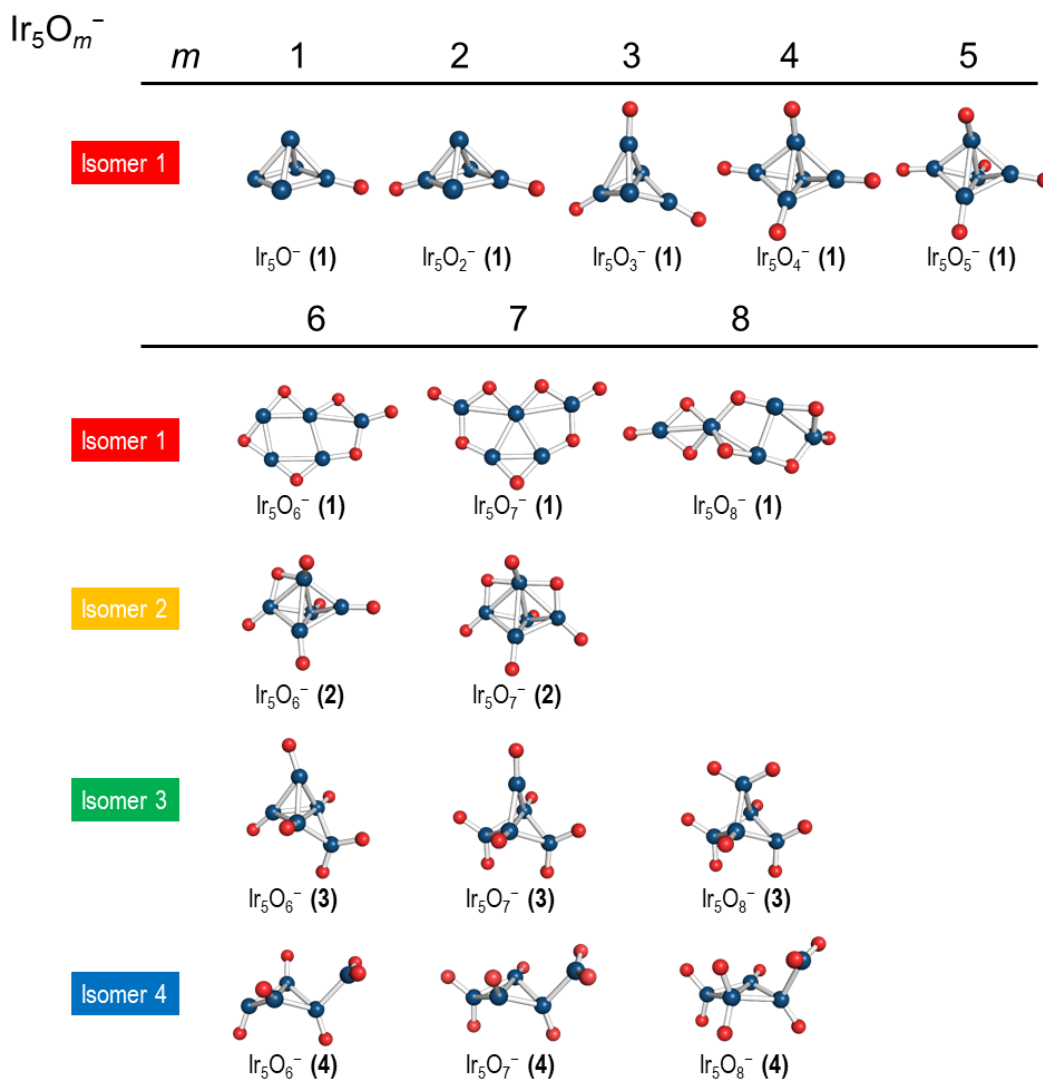
Figure 3.10. Optimized structures of $Ir_5O_m^-$ ($m = 0$–8) obtained by DFT calculation. Navy blue and red spheres represent Ir and O atoms, respectively.

of isomers 2–4 was fixed as quintet. Among these structures, the length of Ir-Ir bond was rarely affected by the on-top bonding of the oxygen. The average length of Ir-Ir in Ir_5^- was 2.65 Å, and those in $Ir_5O_5^-$ and in isomer 4 of $Ir_5O_8^-$ were both 2.64 Å, while that in isomer 1 of $Ir_5O_7^-$ which contained bridged oxygen was 2.89 Å. These result suggested that the Ir-Ir bonds were not elongated by the oxygen atoms bonding to the Ir core as the on-top motif.

Table 3.3. Relative Energies of $Ir_5O_m^-$ (m = 1–8) with Different Spin Multiplicities.[a]

	Spin multiplicity				
	1	3	5	7	9
Ir_5O^- (1)	0.49	0.26	0.16	0	0.06
$Ir_5O_2^-$ (1)	0	0.06	0.27	0.39	0.88
$Ir_5O_3^-$ (1)	0	0.27[b]	0.43[b]	0.76[b]	1.37[b]
$Ir_5O_4^-$ (1)	0.50	0	0.31	0.72	1.35
$Ir_5O_5^-$ (1)	0.18[b]	0.12	0	0.38	1.12[b]
$Ir_5O_6^-$ (1)	0.30	0.15	0	0.14	0.30
$Ir_5O_6^-$ (2)			0.69		
$Ir_5O_6^-$ (3)			0.85		
$Ir_5O_6^-$ (4)			1.26		
$Ir_5O_7^-$ (1)	0.62	0.26	0.24	0	0.20
$Ir_5O_7^-$ (2)			1.22		
$Ir_5O_7^-$ (3)			1.70		
$Ir_5O_7^-$ (4)			1.51		
$Ir_5O_8^-$ (1)	0.62	0	0.00	0.02	0.01
$Ir_5O_8^-$ (3)			0.62		
$Ir_5O_8^-$ (4)			1.13		

[a]Unit in eV. [b]Square pyramidal Ir_5 core.

The calculated CCSs of $Ir_5O_m^-$ are compared with the experimental values in Fig. 3.11 and listed in Table 3.4. In the calibration, the radii of He, Ir^0, Ir^{2+} and O^{2-} were fixed to 1.15, 1.89, 0.84 and 1.32 Å, respectively, so that the calculated CCS values reproduce those of Ir_5^- and $Ir_5O_5^-$. The ratio of the atomic radii of Ir^{2+} to O^{2-} was fixed to 0.89:1.4 as the reference of ionic radii of them in the bulk phase.[51] In this thesis, Ir atoms bonded to O atom in $Ir_nO_m^-$ were treated as Ir^{2+} regardless of the composition, while those not bonded to O atom were treated as Ir^0.
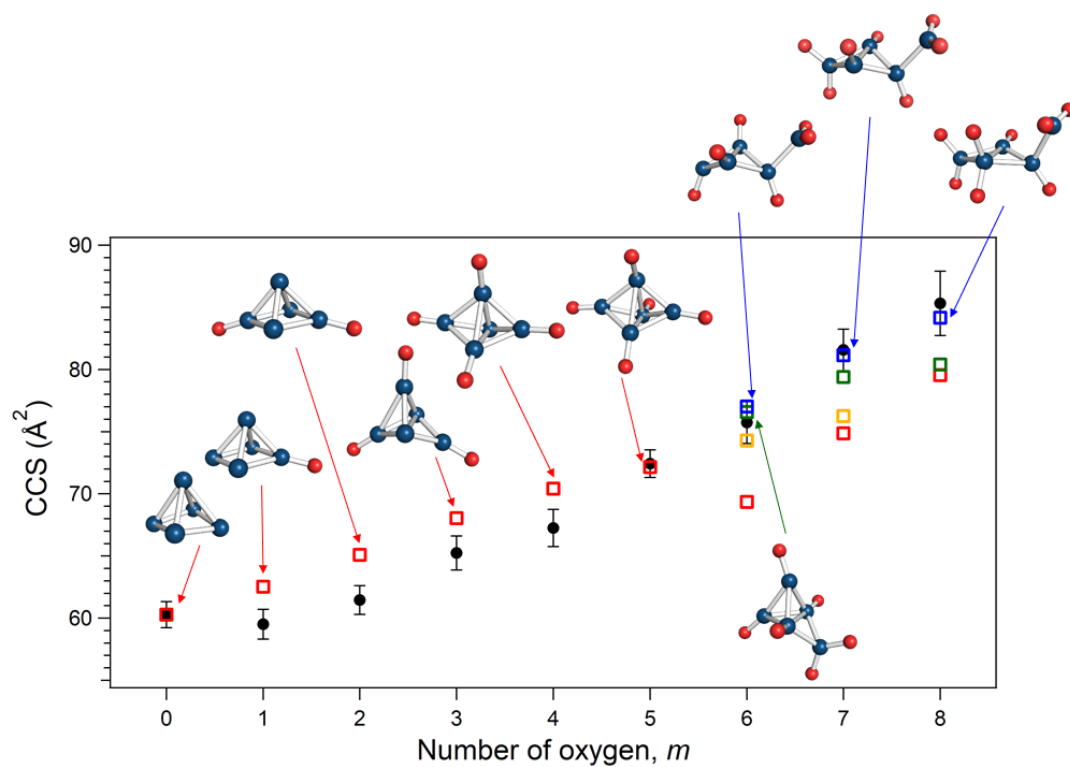
Figure 3.11. CCSs of $Ir_5O_m^-$ as a function of m. Black dots indicate the experimental CCS values. Red, yellow, green and blue squares indicate the calculated CCS values of isomers 1–4, respectively.

Table 3.4. Experimental and Calculated CCS Values of $Ir_5O_m^-$ ($m = 0$–8).[a]

m	0	1	2	3	4
Exp.	60.3±1.1	59.5±1.2	61.5±1.2	65.2±1.4	67.3±1.5
Calc. (Isomer 1)	60.29	62.52	65.08	68.04	70.41
m	5	6	7	8	
Exp.	72.4±1.1	75.7±1.7	81.6±1.7	85.3±2.6	
Calc. (Isomer 1)	72.14	69.35	74.86	79.54	
Calc. (Isomer 2)		74.29	76.25		
Calc. (Isomer 3)		76.57	79.40	80.40	
Calc. (Isomer 4)		77.03	81.15	84.17	

[a]Unit in Å^2.

Experimental CCSs are increased monotonically with increasing m within the accuracy of the measurement up to $m = 8$. Monotonic increase of the experimental CCSs of $Ir_5O_m{}^-$ in the range of $m = 1$–5 are reproduced by the calculated CCS values for the most stable isomers 1. This indicates that oxygen atoms prefer on-top bonding on the terminal sites of Ir_5 core. In contrast, the experimental CCSs of $Ir_5O_m{}^-$ in the range of $m = 6$–8 are reproduced well by the calculated CCSs of the structures with only on-top oxygen (isomers 3 and 4) rather than those with bridged oxygen (isomers 1 and 2). This comparison indicates that the O atoms in $Ir_5O_m{}^-$ ($m = 6$–8) also prefer on-top binding motifs rather than bridged binding motifs.

In the region of $m = 1$ to 4, calculated CCSs were slightly larger than the experimental values. A possible reason for this result is the assumption that Ir atoms in $Ir_5O_m{}^-$ take either form of Ir^0 and Ir^{2+}. However, the analysis of the NBO charge (Table 3.5) indicates that Ir atoms can take intermediate oxidation states. Effective radius of the Ir atoms presumably shrink with increase of the number of oxygen atoms due to electron transfer from Ir to O, leading to the overestimation of the CCS values in the present calculation. Since it is not trivial to calculate the exact CCSs values of metal oxide clusters, I limited myself to semi-quantitative analysis of the CCSs values.

**Table 3.5.** Average Value of NBO Charge on Ir Bonded to O, Ir Not Bonded to O and O in $Ir_5O_m{}^-$ ($m = 0$–5).

m	0	1	2	3	4	5
Ir (bonded to O)		0.284	0.288	0.314	0.336	0.351
Ir (not bonded to O)	−0.2	−0.167	−0.118	−0.130	−0.070	
O		−0.616	−0.610	−0.561	−0.568	−0.551

3.3.2.2. $Ir_8O_m^-$

Optimized structures of several isomers of $Ir_8O_m^-$ obtained by DFT calculation were shown in Fig. 3.12. Relative energies of isomers with different spin multiplicities in each n are compared in Table 3.6. Calculated isomers are categorized into 4 categories; isomer 1: cubic Ir_8 with on-top O, isomer 2: open cubic Ir_8 with bridging O, isomer 3: cubic Ir_8 with bridging O, isomer 4: sheet like Ir_8 with bridging O.

The experimental and calculated CCSs are compared in Fig. 3.13 and Table 3.7. The calibration was conducted by using the CCSs of Ir_8^- and $Ir_5O_5^-$: the radii of He, Ir^0, Ir^{2+} and O^{2-} were fixed to 1.15, 1.91, 0.84 and 1.32 Å, respectively. Experimental CCSs were increased monotonically with m up to $m = 10$, but $Ir_8O_{11}^-$ contained a more compact isomer. In $m \geq 12$, the CCS values were slightly increased again with increase in m. The comparison between experimental and calculated CCSs suggested that oxygen atoms were bonded to the terminal site of the Ir_8 core as on-top motif in $m \leq 11$ as in the case of $Ir_5O_m^-$ ($m \leq 5$). Cubic Ir_8 structure with bridging oxygen did not reproduced the experimental results because their CCS values are much smaller than the structures in Fig. 3.12. The cubic Ir_8 core was retained during sequential oxidation up to $m = 6$ and cubic core motif got distorted from $m = 7$.

Experimental CCSs were suddenly decreased at $m = 11$. As shown in Figure 3.13, such small CCSs are explained by isomer 2 having open-cube structure with bridging oxygen structure (Fig. 3.12). Bridging oxygen motif was also predicted previously for oxygen rich species such as Ir_8O_{16}.[14] The assignment leads us to conclude that oxygen binding motif was changed from on-top to bridging (μ_2), and the boundary was $m = 11$ at which two isomers coexist. Oxygen atoms bind to the Ir core one by one up to $m = n$, and additional oxygen atoms cause the distortion of the Ir core. In the more oxygen-rich
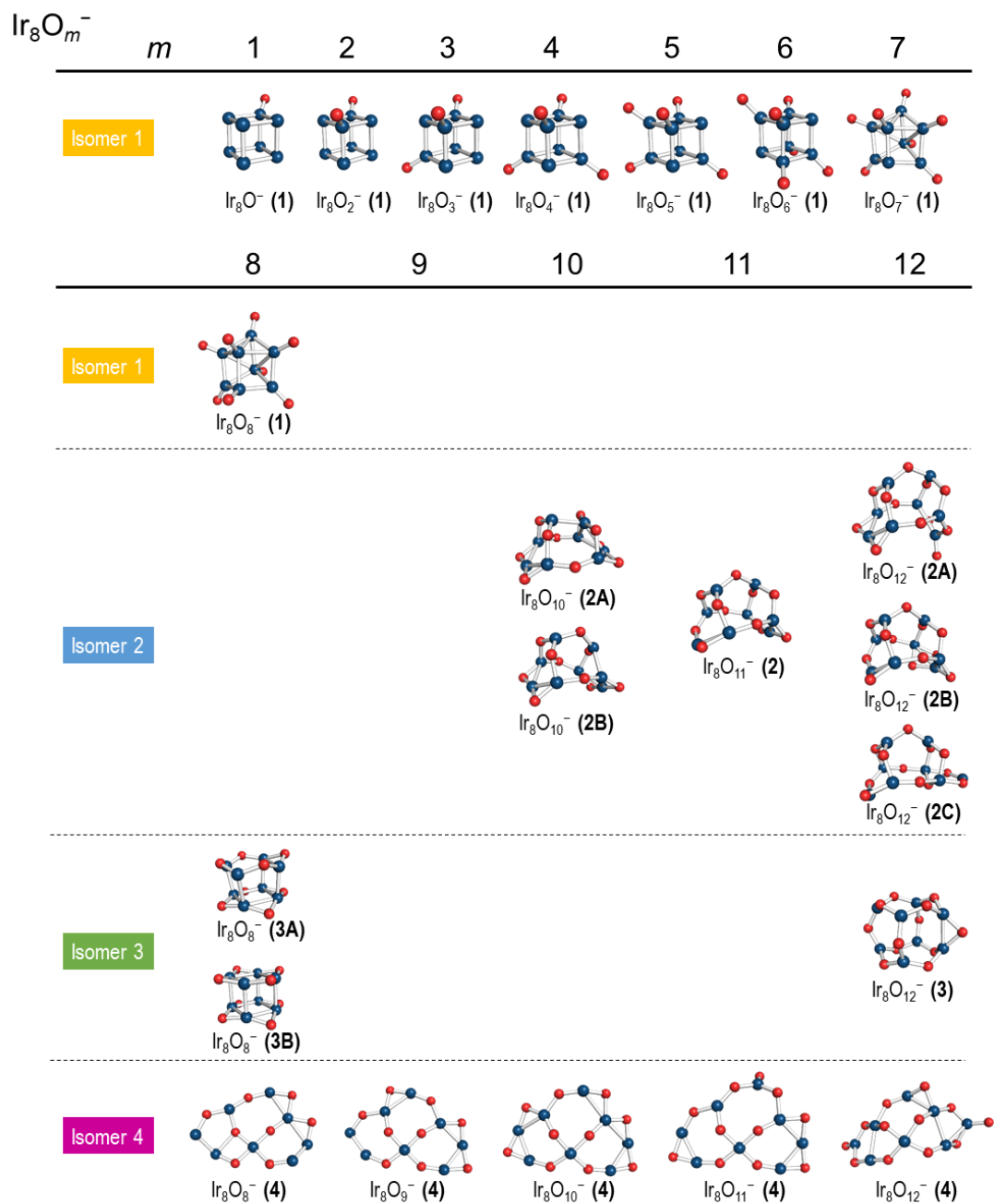
Figure 3.12. Optimized structures of $Ir_8O_m^-$ ($m = 0\text{–}12$) obtained by DFT calculation. Navy blue and red spheres represent Ir and O atoms, respectively.

Table 3.6. Relative Energies of $Ir_8O_m^-$ (m = 1–12) with Different Spin Multiplicities.[a]

	Spin multiplicity				
	2	4	6	8	10
Ir_8O^- **(1)**	0.07	0.13	0	0.01	0.01
$Ir_8O_2^-$ **(1)**	0.17	0.01	0	0.02	0.13
$Ir_8O_3^-$ **(1)**	0.18	0.14	0	0.18	0.93
$Ir_8O_4^-$ **(1)**	0.14	0.13	0	0.98	1.79
$Ir_8O_5^-$ **(1)**	0.03	0	0.06	0.62	1.37
$Ir_8O_6^-$ **(1)**	0	0.29	0.70	1.17	1.77
$Ir_8O_7^-$ **(1)**	0	0.53	0.71	0.92	1.33
$Ir_8O_8^-$ **(1)**	0.35	0.85	1.14	1.53	2.13
$Ir_8O_8^-$ **(3A)**	0	0.27	0.06	0.13	0.34
$Ir_8O_8^-$ **(3B)**	0.77	0.84	0.92	0.40	1.73
$Ir_8O_8^-$ **(4)**	4.42	4.52	4.88	4.64	4.46
$Ir_8O_9^-$ **(4)**	0.14	0.35	0.40	0.77	0
$Ir_8O_{10}^-$ **(2A)**	0.71	0.64	0.88	0.70	0.59
$Ir_8O_{10}^-$ **(2B)**	0.27	0	0.58	1.13	1.12
$Ir_8O_{10}^-$ **(4)**	0.62	0.62	1.18	1.33	1.53
$Ir_8O_{11}^-$ **(2)**	0.41	0.19	0	0.34	0.59
$Ir_8O_{11}^-$ **(4)**	0.79	0.79	0.62	1.12	0.58
$Ir_8O_{12}^-$ **(2A)**	0.47	0.53	0.93	0.86	1.27
$Ir_8O_{12}^-$ **(2B)**	0.95	1.23	1.70	1.66	[b]
$Ir_8O_{12}^-$ **(2C)**	1.74	1.96	2.23	2.221	2.73
$Ir_8O_{12}^-$ **(3)**	0.16	0	0.14	0.70	1.07
$Ir_8O_{12}^-$ **(4)**	0.73	1.63	0.90	1.90	2.38

[a]Unit in eV. [b]Structure was transformed to different motif during the optimization.
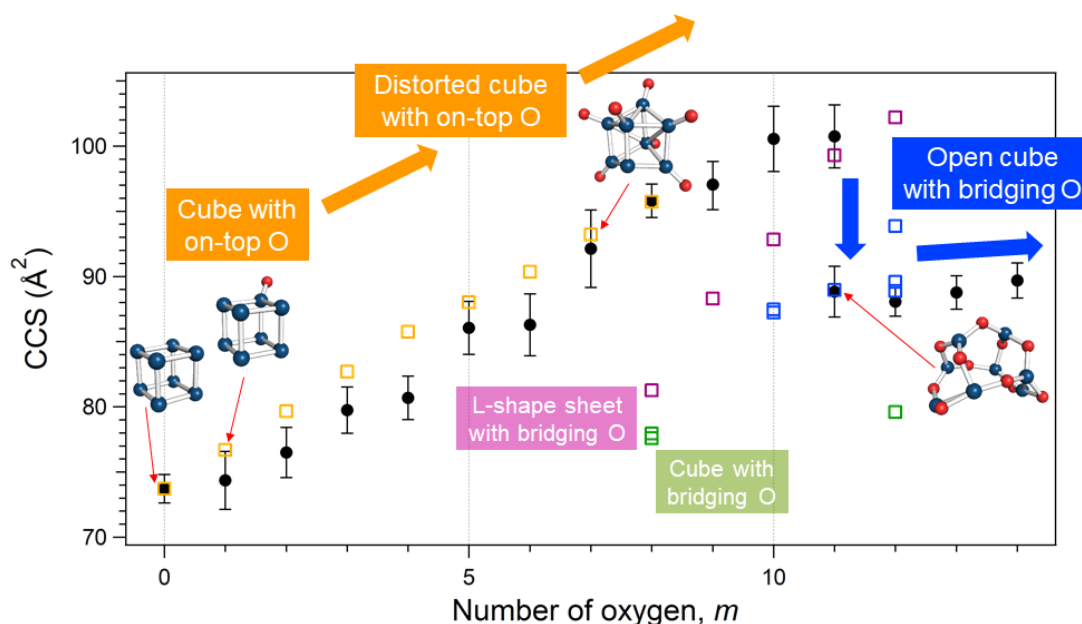
Figure 3.13. CCSs of $Ir_8O_m^-$ ($m = 0$–14). Black circles indicate the experimental value. Orange, blue, green and purple squares indicate the calculated CCS values of isomers 1–4, respectively.

clusters, bridging oxygen motif became more stable because the on-top motif demanded a large distortion of the Ir core probably due to the steric effect. Sheet-like structures with bridged oxygen atoms were also calculated as other candidates. The CCS values of sheet like structure could explain the experimental CCS values only for $Ir_8O_{11}^-$. This structural transition was commonly observed in $n \geq 8$. As already mentioned, the core structure was significantly distorted at $m \geq n$. When core distortion become large, the structure was changed from the compact cubic structure to sheet-like structure such as isomer 4 of $Ir_5O_8^-$. When the number of atoms in the cluster is large, sheet-like structure is thought to be unfavorable due to large surface energy. In the case of Au_n^-, 3D structures were favored in $n \geq 12$, while 2D structures were preferred in $n \leq 12$.[46,52,53] Therefore, in the case of $n \geq 8$ with large m, μ_2-O structure was more stable than on-top O structure with distorted core.

73

Table 3.7. Experimental and Calculated CCS Values of $Ir_8O_m^-$ (m = 0–14).[a]

| m	0	1	2	3	4
Exp.	73.7±1.1	74.4±2.2	76.5±1.9	79.7±1.8	80.7±1.7
Calc. (Isomer 1)	73.72	76.69	79.67	82.70	85.76
m	5	6	7	8	9
Exp.	86.0±2.0	86.3±2.4	92.1±3.0	95.8±1.3	97.0±1.9
Calc. (Isomer 1)	88.03	90.36	93.23	95.72	
Calc. (Isomer 3A)				77.95	
Calc. (Isomer 3B)				77.60	
Calc. (Isomer 4)				81.27	88.30
m	10	11	12	13	14
Exp.	100.6±2.5	88.8±1.9	88.1±1.1	88.8±1.3	89.7±1.3
Exp. (2)		100.7±2.4			
Calc. (Isomer 2A)	87.46	88.97	93.85		
Calc. (Isomer 2B)	87.24		89.58		
Calc. (Isomer 2C)			88.89		
Calc. (Isomer 3)			79.60		
Calc. (Isomer 4)	92.84	99.30	102.20		

[a]Unit in $Å^2$.

3.3.3. Comparison of the O binding structure with Co clusters

According to the above results, iridium oxide clusters with the small oxygen ratio (O/Ir < ~1.5) showed the on-top oxygen binding motif, while typical transition metal clusters in the previous experiment showed the μ_2 or μ_3 bridging binding motif. For example, oxygen atoms were sequentially bonded to the bridge or hollow sites of Co_7 core as shown in Chapter 2. This remarkable difference in the binding motifs are explained by the shape of frontier orbitals of the clusters involved in the bonding. Fig. 3.14 shows the HOMO of the optimized structures of the Co_7^- and Ir_8^-. The HOMO of Ir_8^- is localized on terminal sites, while that of Co_7^- is distributed over the hollow sites. This difference in the shapes of HOMO caused the different bonding motif of the oxygen onto the Ir and Co clusters.

From the viewpoint of the core structure, Ir-Ir bond in the cubic Ir_8 was retained compared to the Co oxide clusters. As mentioned in Chapter2, the Co-Co bonds were elongated by attaching the oxygen atoms to the bridge/hollow site of the Co core. The average length of Co-Co bonds was elongated from 2.49 Å in Co_7^- to 2.84 Å in $Co_7O_6^-$. On the other hand, the length of Ir-Ir bond was almost retained after the attachment of the oxygen to the terminal site as mentioned in Section 3.3.2.1. The average length of Ir-Ir bonds was 2.65 Å in Ir_5^- and 2.64 Å in the on-top isomer (isomer 4) of $Ir_5O_8^-$, while that was elongated to 2.89 Å in the bridging isomer (isomer 1) of $Ir_5O_7^-$. These result suggested that the on-top binding motif of oxygen atoms did not elongate the metal-metal bonds. As a result, $Ir_8O_m^-$ kept the cubic Ir_8 core structure in $m \leq 6$. In $m \geq 7$, Ir core was gradually distorted.
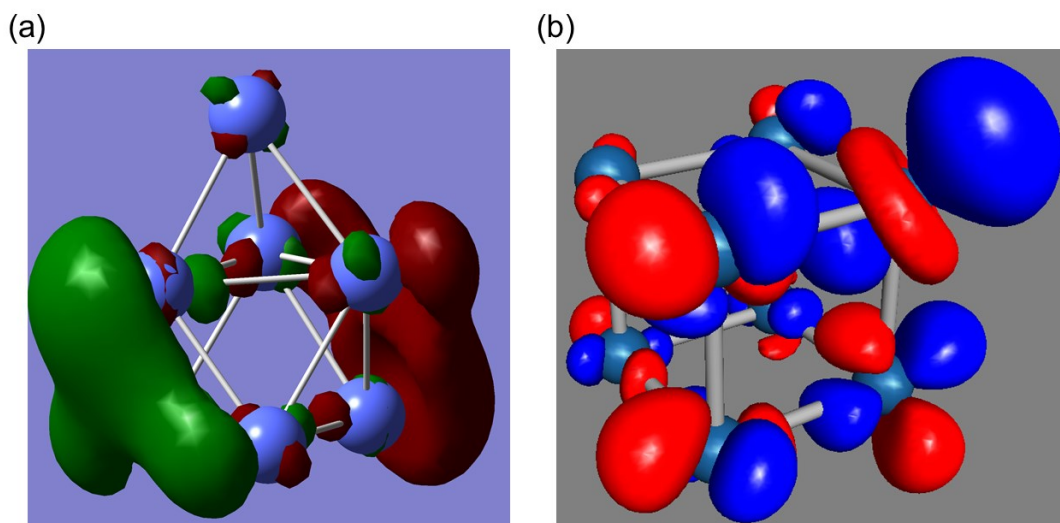
Figure 3.14. HOMO of the (a) Co_7^- (15tet) and (b) Ir_8^- (6tet).

3.4. Conclusions

The structures of $Ir_nO_m^-$ produced by the laser ablation under O_2 seeded He were examined by using ion mobility mass spectrometry and theoretical calculations. Oxygen atoms in $Ir_nO_m^-$ were bonded to the terminal site of the Ir core as on-top configuration when $m \leq n$. In $m \geq n$ region, on-top configuration was basically favored although Ir core got distorted with increasing the number of O atoms. However, in $n \geq 8$, the μ_2 configuration of oxygen to bridge site of the Ir core was more favored than on-top configuration, for example at $m > 11$ and $n = 8$. Theoretical calculations suggested that this structural transition of oxygen bonding motif resulted from the large distortion of the Ir core induced by sequential oxygen binding.

References

1. Mafuné, F.; Takenouchi, M.; Miyajima, K.; Kudoh, S. *J. Phys. Chem. A* **2016**, *120*, 356.

2. Koyama, K.; Nagata, T.; Kudoh, S.; Miyajima, K.; Huitema, D. M. M.; Chernyy, V.; Bakker, J. M.; Mafune, F. *J. Phys. Chem. A* **2016**, *120*, 8599.

3. Ohshimo, K.; Komukai, T.; Moriyama, R.; Misaizu, F. *J. Phys. Chem. A* **2014**, *118*, 3899.

4. Ota, K.; Koyasu, K.; Ohshimo, K.; Misaizu, F. *Chem. Phys. Lett.* **2013**, *588*, 63.

5. Ohshimo, K.; Azuma, S.; Komukai, T.; Moriyama, R.; Misaizu, F. *J. Phys. Chem. C* **2015**, *119*, 11014.

6. Koyasu, K.; Komatsu, K.; Misaizu, F. *J. Chem. Phys.* **2013**, *139*, 164308.

7. Ohshimo, K.; Norimasa, N.; Moriyama, R.; Misaizu, F. *J. Chem. Phys.* **2016**, *144*, 194305.

8. Wu, J. W. J.; Moriyama, R.; Tahara, H.; Ohshimo, K.; Misaizu, F. *J. Phys. Chem. A* **2016**, *120*, 3788.

9. Moriyama, R.; Sato, R.; Nakano, M.; Ohshimo, K.; Misaizu, F. *J. Phys. Chem. A* **2017**, *121*, 5605.

10. Wu, J. W. J.; Moriyama, R.; Nakano, M.; Ohshimo, K.; Misaizu, F. *Phys. Chem. Chem. Phys.* **2017**, *19*, 24903.

11. Fielicke, A.; Meijer, G.; Von Helden, G. *Eur. Phys. J. D* **2003**, *24*, 69.

12. Asmis, K. R.; Sauer, J. *Mass Spectrom. Rev.* **2007**, *26*, 542.

13. Zhou, X.; Yang, J.; Li, C. *J. Phys. Chem. A* **2012**, *116*, 9985.

14. Halder, A.; Liu, C.; Liu, Z.; Emery, J. D.; Pellin, M. J.; Curtiss, L. A.; Zapol, P.; Vajda, S.; Martinson, A. B. F. *J. Phys. Chem. C* **2018**, *122*, 9965.

15. Zhang, W.; Xiao, L.; Hirata, Y.; Pawluk, T.; Wang, L. *Chem. Phys. Lett.* **2004**, *383*, 67.

16. Bussai, C.; Krüger, S.; Vayssilov, G. N.; Rösch, N. *Phys. Chem. Chem. Phys.* **2005**, *7*, 2656.

17. Pawluk, T.; Hirata, Y.; Wang, L. *J. Phys. Chem. B* **2005**, *109*, 20817.

18. Zhang, M.; Fournier, R. *Phys. Rev. A* **2009**, *79*, 043203.

19. Hu, C. H.; Chizallet, C.; Toulhoat, H.; Raybaud, P. *Phys. Rev. B* **2009**, *79*, 195416.

20. Du, J.; Sun, X.; Chen, J.; Jiang, G. *J. Phys. Chem. A* **2010**, *114*, 12825.

21. Chen, Y.; Huo, M.; Chen, T.; Li, Q.; Sun, Z.; Song, L. *Phys. Chem. Chem. Phys.* **2015**, *17*, 1680.

22. Jorge, F. E.; Venancio, J. R. da C. *Chinese Phys. B* **2018**, *27*, 063102.

23. Rumble, J. R. *CRC Handbook of Chemistry and Physics*, 98th ed.; CRC Press: Boca Raton, 2017.

24. Sharif, M. J.; Maity, P.; Yamazoe, S.; Tsukuda, T. *Chem. Lett.* **2013**, *42*, 1023.

25. Higaki, T.; Kitazawa, H.; Yamazoe, S.; Tsukuda, T. *Nanoscale* **2016**, *8*, 11371.

26. Yamamoto, H.; Maity, P.; Takahata, R.; Yamazoe, S.; Koyasu, K.; Kurashige, W.; Negishi, Y.; Tsukuda, T. *J. Phys. Chem. C* **2017**, *121*, 10936.

27. Wang, L.; Ge, Q. *Chem. Phys. Lett.* **2002**, *366*, 368.

28. Zhang, W.; Zhao, H.; Wang, L. *J. Phys. Chem. B* **2004**, *108*, 2140.

29. Bae, Y. C.; Kumar, V.; Osanai, H.; Kawazoe, Y. *Phys. Rev. B* **2005**, *72*, 125427.

30. Li, S.; Li, H.; Liu, J.; Xue, X.; Tian, Y.; He, H.; Jia, Y. *Phys. Rev. B* **2007**, *76*, 045410.

31. Lee, S.; Fan, C.; Wu, T.; Anderson, S. L. *J. Phys. Chem. B* **2005**, *109*, 381.

32. Okrut, A.; Runnebaum, R. C.; Ouyang, X.; Lu, J.; Aydin, C.; Hwang, S. J.; Zhang, S.; Olatunji-Ojo, O. A.; Durkin, K. A.; Dixon, D. A.; Gates, B. C.; Katz, A. *Nat. Nanotechnol.* **2014**, *9*, 459.

33. Mason, E. A. and McDaniel, E. W. *Transport Properties of Ions in Gases*; Wiley and Sons: New York, 1988.

34. Weis, P. *Int. J. Mass Spectrom.* **2005**, *245*, 1.

35. Ohshimo, K.; Komukai, T.; Takahashi, T.; Norimasa, N.; Wu, J. W. J.; Moriyama, R.; Koyasu, K.; Misaizu, F. *Mass Spectrom.* **2014**, *3*, S0043.

36. Krylov, E.; Nazarov, E. G.; Miller, R. A.; Tadjikov, B.; Eiceman, G. A. *J. Phys. Chem. A* **2002**, *106*, 5437.

37. Dugourd, P.; Hudgins, R. R.; Clemmer, D. E.; Jarrold, M. F. *Rev. Sci. Instrum.* **1997**, *68*, 1122.

38. Schäfer, A.; Horn, H.; Ahlrichs, R. *J. Chem. Phys.* **1992**, *97*, 2571.

39. Eichkorn, K.; Weigend, F.; Treutler, O.; Ahlrichs, R. *Theor. Chem. Acc.* **1997**, *97*, 119.

40. Eichkorn, K.; Treutler, O.; Öhm, H.; Häser, M.; Ahlrichs, R. *Chem. Phys. Lett.* **1995**, *240*, 283.

41. *TURBOMOLE*, V7.2, University of Karlsruhe and Forschungszentrum Karlsruhe GmbH (1989–2007) and TURBOMOLE GmbH (since 2007), 2017; available from http://www.turbomole.com (accessed Dec. 2018).

42. *The PyMOL Molecular Graphics System*, version 1.8; Schrödinger, LLC.

43. von Helden, G.; Hsu, M. T.; Gotts, N.; Bowers, M. T. *J. Phys. Chem.* **1993**, *97*, 8182.

44. Mesleh, M. F.; Hunter, J. M.; Shvartsburg, A. A.; Schatz, G. C.; Jarrold, M. F. *J. Phys. Chem.* **1996**, *100*, 16082.; Erratum, *J. Phys. Chem. A* **1997**, *101*, 968.

45. Shvartsburg, A. A.; Jarrold, M. F. *Chem. Phys. Lett.* **1996**, *261*, 86.

46. Furche, F.; Ahlrichs, R.; Weis, P.; Jacob, C.; Gilb, S.; Bierweiler, T.; Kappes, M. M. *J. Chem. Phys.* **2002**, *117*, 6982.

47. Lerme, J.; Dugourd, P.; Hudgins, R. R.; Jarrold, M. F. *Chem. Phys. Lett.* **1999**, *304*, 19.

48. Armbruster, M. K.; Weigend, F.; Van Wüllen, C.; Klopper, W. *Phys. Chem. Chem. Phys.* **2008**, *10*, 1748.

49. Kelting, R.; Otterstätter, R.; Weis, P.; Drebov, N.; Ahlrichs, R.; Kappes, M. M. *J. Chem. Phys.* **2011**, *134*, 024311.

50. Tono, K.; Terasaki, A.; Ohta, T.; Kondow, T. *J. Chem. Phys.* **2003**, *119*, 11221.

51. Dean, J. A. *Lange's Handbook of Chemistry*, 13th ed.; McGraw-Hill, Inc.: New York, 1985.

52. Häkkinen, H.; Yoon, B.; Landman, U.; Li, X.; Zhai, H. J.; Wang, L. S. *J. Phys. Chem. A* **2003**, *107*, 6168.

53. Wang, L.-M.; Wang, L.-S. *Nanoscale* **2012**, *4*, 4038.

Chapter 4.

Concluding Remarks

Aiming at gaining an insight onto the oxygen adsorption step of oxidation reactions catalyzed by metal clusters, I focused on the initial stage of oxidation reaction of the metal clusters. In this thesis, I investigated the geometric and electronic structure of the metal oxide cluster anions produced by the sequential oxidation reactions by using several experimental and theoretical methods.

In Chapter 2, I studied the oxidation reaction of the cobalt cluster anions by using mass spectrometry, photoelectron spectroscopy and DFT calculations. Two types of magic behaviors were observed in mass spectra of $Co_nO_m^-$; the intensity abruptly increased and decreased at certain compositions **U** and **D**, respectively. The species **U** showed drastic increase of the AEA values according to the PES results. It indicated that the magic species **U** resulted from the thermionic electron emission. Magic species **D** could be separated to two, one appeared in $n{:}m \sim 1{:}1$ and the other appeared in $n{:}m \sim 3{:}4$. DFT calculations suggested that former one was attributed to the surface oxidized species. Latter one was thought to be a fully oxidized species because of the stoichiometry.

In Chapter 3, I investigated the oxidation reaction of the iridium cluster anions by using mass spectrometry, ion mobility spectroscopy and theoretical calculations. According to the results of ion mobility spectrometry of $Ir_nO_m^-$, oxygen atoms were bonded to cubic-like Ir core as an on-top motif at $m \leq n$. At $m \geq n$, the oxygen was bonded as an on-top motif but Ir core was strongly distorted. Especially $n \geq 8$, the bonding motif transition was observed: on-top to bridge transition due to the core distortion by sequential oxygen binding.

In these chapters, I investigated the oxidation reactions on two types of metal clusters. The biggest difference observed in this thesis is the oxygen bonding motif. In the case of Co, oxygen atoms were bonded to the bridging site or facet site as μ_2 or μ_3 motif, while

Ir oxide clusters showed on-top motif at terminal site. The possible reason of this difference is the stability of the metal core. The structure of the metal core is different between Co and Ir. Cubic feature can be seen in the Ir clusters, whereas Co clusters form the more compact structure such as octahedron. In the present thesis, simple cubic structure was retained up to $m = 6$ in the case of $Ir_8O_m^-$ as increasing oxygen atoms, while the Co core was expanded by the oxidation. On the basis of this comparison, it is thought that the iridium clusters preferred the on-top oxygen binding motif rather than bridging motif in order to keep the cubic structure. DFT calculation of $Ir_nO_m^-$ isomers showed the elongation of Ir-Ir bond by bonding μ_2 oxygen and it supports the hypothesis.

In conclusion, I demonstrated throughout Chapters 2 and 3 that Co and Ir showed the different behavior during the sequential oxidation reaction. These two types of the oxygen bonding motif can affect the reactions of the metal oxide clusters including catalytic reactions. For further study, the research on oxygen environment of the Ir and Co oxide clusters and their core motifs can help the explanation of the phenomena such as mechanism and difference of the reactivity from the viewpoint of the cluster structures. In addition, other elements in platinum elements such as Ru and Os also have the possibility to have the on-top oxygen binding motif because they also prefer cubic structure.[1–4] The stability of cubic structure differs among the elements. Therefore, the size-dependency of the oxygen binding motif and core distortion may be tuned by changing elements. It can be a new guideline to control the structure of the oxide clusters and bonding nature of oxygen.

References

1. Zhang, W.; Xiao, L.; Hirata, Y.; Pawluk, T.; Wang, L. *Chem. Phys. Lett.* **2004**, *383*, 67.

2. Zhang, W.; Zhao, H.; Wang, L. *J. Phys. Chem. B* **2004**, *108*, 2140.

3. Zhang, M.; Fournier, R. *Phys. Rev. A* **2009**, *79*, 043203.

4. Hu, C. H.; Chizallet, C.; Toulhoat, H.; Raybaud, P. *Phys. Rev. B* **2009**, *79*, 195416.

List of Publications and Presentations

Publications related to the thesis

(Chapter 2)

1. "Observation and the Origin of Magic Compositions of $Co_nO_m^-$ Formed in Oxidation of Cobalt Cluster Anions",
   <u>Ryohei Tomihara</u>, Kiichirou Koyasu and Tatsuya Tsukuda, *J. Phys. Chem. C*, **2017**, *121*, 10957–10963.
2. "コバルトクラスター負イオンの酸化過程における $Co_nO_m^-$ の魔法組成の出現とその起源",
   <u>冨原 良平</u>, 小安 喜一郎, 佃 達哉, ナノ学会会報, **2017**, *16*, 7–13.

Publications not related to the thesis

1. "Collision-Induced Dissociation of Undecagold Clusters Protected by Mixed Ligands $[Au_{11}(PPh_3)_8X_2]^+$ (X = Cl, C≡CPh)",
   <u>Ryohei Tomihara</u>, Keisuke Hirata, Hiroki Yamamoto, Shinjiro Takano, Kiichirou Koyasu and Tatsuya Tsukuda, *ACS Omega*, **2018**, *3*, 6237–6242.
2. "N-Heterocyclic Carbene-Functionalized Magic Number Gold Nanoclusters",
   Mina R. Narouz, Kimberly M. Osten, Phillip J. Unsworth, Renee W. Y. Man, Kirsi Salorinne, Shinjiro Takano, <u>Ryohei Tomihara</u>, Sami Kaappa, Sami Malola, Cao-Thang Dinh, J. Daniel Padmos, Kennedy Ayoo, Patrick J. Garrett, Masakazu Nambo, J. Hugh Horton, Edward H. Sargent, Hannu Häkkinen, Tatsuya Tsukuda and Cathleen M. Crudden, *Nature Chemistry*, accepted for publication.

Oral presentations

1. "Detection and characterization of surface oxidized cobalt clusters",

   ◯Ryohei TOMIHARA, Kiichirou KOYASU, Tatsuya TSUKUDA, The 97th CSJ Annual Meeting, Keio university, Kanagawa, March 2017.

2. "Collision induced dissociation of phosphine-protected gold clusters, $[Au_{11}(PPh_3)_8X_2]^+$ (X=Cl, C_2Ph)",

   ◯Ryohei TOMIHARA, Hiroki YAMAMOTO, Shinjiro TAKANO, Kiichirou KOYASU, Tatsuya TSUKUDA, The 98th CSJ Annual Meeting, Nihon University, Chiba, March 2018.

(to be scheduled)

1. "Structural transition in the sequential oxidation of iridium cluster anions revealed by ion mobility measurements",

   ◯Ryohei TOMIHARA, Toshiaki NAGATA, Jenna WU W. J., Kiichirou KOYASU, Motoyoshi NAKANO, Keijiro OHSHIMO, Fuminori MISAIZU, Tatsuya TSUKUDA, The 99th CSJ Annual Meeting, Konan University, Hyogo, March 2019.

Poster presentations

1. "耐酸化性コバルト酸化物クラスター負イオンの生成とその構造評価",
   ○冨原良平, 小安喜一郎, 佃達哉, ナノ学会第14回大会, 北九州国際会議場, 福岡, 2016 年 6 月.
   (Young best presentation award)

2. "高い酸化耐性をもつコバルト酸化物クラスターの探索と構造評価",
   ○冨原良平, 小安喜一郎, 佃達哉, 第10回分子科学討論会, 神戸ファッションマート, 兵庫, 2016 年 9 月.

3. "酸化コバルトクラスターの安定組成の探索とその構造解析",
   ○冨原良平, 小安喜一郎, 佃達哉, 第 6 回 CSJ 化学フェスタ 2016, タワーホール船堀, 東京, 2016 年 11 月.

4. "In-source CID measurement of thiolate-protected gold clusters",
   ○Ryohei Tomihara, Shinjiro Takano, Seiji Yamazoe, Kiichirou Koyasu, Tatsuya Tsukuda, International Symposium on Monolayer-Protected Clusters 2017 (ISMPC17), Monte Verità, Ascona/Switzerland, August 2017.
   (Award for the best poster)

5. "配位子保護金属クラスターのインソース衝突誘起解離",
   ○冨原良平, 高野慎二郎, 山添誠司, 小安喜一郎, 佃達哉, 第 11 回分子科学討論会, 東北大学, 宮城, 2017 年 9 月.

6. "In-source Collision Induced Dissociation Measurement of Undecagold Clusters $[Au_{11}(PPh_3)_8X_2]^+$ (X=Cl,C$_2$Ph)",
   ○Ryohei TOMIHARA, Hiroki YAMAMOTO, Shinjiro TAKANO, Kiichirou KOYASU, Tatsuya TSUKUDA, Asian Symposium on Nanoscience and Nanotechnology 2018 (ASNANO2018), Tokyo, Japan, May 2018.

7. "Collision-induced dissociation mass spectrometry on the gold clusters protected by mixed ligands, $[Au_{11}(PPh_3)_8X_2]^+$ (X=Cl and C≡CPh)",
   ○R. Tomihara, K. Hirata, H. Yamamoto, S. Takano, K. Koyasu, T. Tsukuda, The 19th International Symposium on Small Particles and Inorganic Clusters (ISSPIC-XIX), Hangzhou, China, August 2018.

8. "Ir 酸化物クラスター負イオンのイオン移動度測定：酸化の進行に伴う構造モチーフの転換",
   ○冨原良平, 永田利明, Wu Jenna W. J., 小安喜一郎, 中野元善, 大下慶次郎, 美齊津文典, 佃達哉, 第 12 回分子科学討論会, 福岡国際会議場, 福岡, 2018 年 9 月.

Acknowledgements

I would like to show my greatest appreciation to Prof. Tsukuda for educating and training me as a scientist. He taught me not only the techniques and the knowledge for science, but also behavior, a manner to discuss, writing rules of a paper and an application document and a way to use scientific English. Lessons learned in the Lab. will help me in the life of a scientist and he is a model of the best scientist.

I express my sincere thanks to Associate Prof. Kiichirou Koyasu for his instructions in my whole gas-phase research. I learned much about manners of the study on physical chemistry from his techniques on experiment and calculation and wonderful advises. I could not have conducted my research without his cooperations.

I am grateful to Prof. Seiji Yamazoe in Tokyo Metropolitan Univ. and Assistant Prof. Shinjiro Takano in our Lab. for giving advises on my research especially related to the synthesis and the analysis based on their wide knowledge on chemical materials and catalysts. In some works, they provided the samples of the ligand-protected clusters synthesized in liquid phase with high quality.

I owe a deep debt of gratitude to Prof. Fuminori Misaizu in Tohoku Univ. and his lab-members for the collaboration works in ion-mobility spectrometry experiment (Chapter 3). Notably, Assistant Prof. Keijiro Ohshimo, Assistant Prof. Motoyoshi Nakano, Dr. Toshiaki Nagata and Dr. Jenna W. J. Wu supported me in the experiment and analysis. I was able to spend productive time in Sendai thanks to their warm hospitality. I also appreciate the fruitful discussions about the study.

<div align="right">Ryohei Tomihara</div>